Discrete differential geometry of fluvial landscapes

Nathaniel Klema[1,2], Leif Karlstrom[2], and Joshua Roering[2]

[1]Department of Physics and Engineering, Fort Lewis College,Durango, Colorado 81301, U.S.A.
[2]Department of Earth Sciences, University of Oregon, Eugene, Oregon 97403, U.S.A

Correspondence: Nathaniel Klema (ntklema@fortlewis.edu)

Abstract. Geomorphology as a discipline is ~~often~~ defined by the use of topographic ~~geometry~~ form to understand surface processes on Earth and other planets. In practice this requires drawing ~~quantitative connections between~~ connections between quantitative metrics of surface geometry and rates of exhumation, to understand the spatial partitioning of different erosion processes and the ~~feedbacks~~ feedback between them. Curvature, ~~among~~ perhaps the most fundamental ~~ways~~ way to measure and categorize surfaces of any kind, also appears ~~in some erosion laws~~ explicitly in many erosion models and is therefore of significance to ~~geomophology~~geomorphology. However, ~~curvature is challenging to compute from~~ there is ambiguity in how curvature of discretely sampled topographic surfaces such as digital elevation models ~~.~~ is defined and calculated. Many landscape evolution studies leverage curvature calculated as the scalar output of the Laplacian operator applied to map-view projections, which approximates but can deviate significantly from the surface curvature tensor at a point. In this study we use a formal surface theory approach to compute intrinsic and extrinsic curvature metrics, and associated shape-class distributions, of approximate steady-state fluvial topography of the Oregon Coast Range, USA. ~~This~~ We develop a workflow, including careful spectral filtering to isolate wavelengths of interest, that provides a nuanced view of landscape ~~structure,~~ geometry while simultaneously eliminating systematic errors arising from map-view approaches to topographic analysis. ~~We leverage two~~ Two invariants of the curvature tensor ~~at a point~~ – the ~~Mean~~ mean and Gaussian curvatures – ~~to identify novel~~ reveal systematic structure of topographic geometry in channel and ridge networks that ~~captures the full compliment of documented process regime transitions . We show that the Laplacian operator, a commonly used scalar metric of landscape curvature, admits systematic error (up to $\sim 300\%$ percent) when applied directly to map-view topographic projections and should thus be used with caution. Finally, we show remarkable symmetries in the distribution of~~ appears to capture transitions between hillslope, debris flow, and fluvial process regimes. Mean curvature and associated shape classes ~~, specifically an equipartition of the landscape~~ are equipartitioned between concave-down and concave-up elements, forming complementary branching structures that span the landscape. These results suggest that formal surface theory approaches could prove valuable in maximizing the utility of digital elevation data ~~and understanding the processes driving the evolution and organization~~ through differentiation and definition of process regimes that drive the evolution of fluvial landscapes.

1 Introduction

The Earth's surface contains multi-scale signatures of the processes that have shaped it. Over length scales of $10^2 - 10^4$ km, long-wavelength relief ~~generally~~ tracks patterns of lithospheric deformation and ~~isostacy~~ isostasy (Wieczorek, 2015) with relief generally increasing ~~as~~ with the horizontal scale of measurement ~~increases~~ (Turcotte, 1987). The resulting gravitational gradients drive surface erosion ~~, which~~ that shapes the landscape at finer scales (Perron et al., 2008; Hooshyar et al., 2020; Bonetti et al., 2020) through a combination of diffusive (Roering et al., 2001a), advective (Whipple and Tucker, 1999), and stochastic mass transport (Furbish et al., 2009). ~~The rates of these erosion processes can be quantitatively linked to topographic form, and so geometry of the landscape can be used to study the competing long-timescale dynamics of bedrock uplift (Kirby and Whipple, 2012; Klema et al., 2023), and erosion that is modulated by lithology (Stock and Montgomery, 1999), climate (Ferrier et al., 2013), and ecology (Amundson et al., 2015).~~

In the spirit of reductionism, geomorphic studies often ~~isolate~~ focus on regions where a single erosion process is assumed dominant~~, requiring the identification of distinct process regimes~~. There are many established approaches to ~~landscape partitioning (Montgomery and Foufoula-Georgiou, 1993; Shary, 1995; Jasiewicz and Stepinski, 2013), however this approach~~ partitioning the landscape into process domains (Montgomery and Foufoula-Georgiou, 1993; Shary, 1995; Jasiewicz and Stepinski, 2013) . However, compartmentalization comes at the risk of ~~oversimplification~~oversimplifying interactions between processes. For example, the transition from hillslopes to fluvial channels ~~often occurs just below topographic hollows that where shallow landslides tend to initiate and the interactions between end-member process domains have implications for both landscape evolution and hazard prediction (Stock and Dietrich, 2003; Struble et al., 2023). As~~ commonly occurs in topographic hollows where gullies begin to incise. Here, interactions between hillslope and fluvial processes influence both long-term landscape evolution (Perron et al., 2012) and short-term mass motions that are of interest for hazard prediction (Yanites et al., 2025; Struble et al., 202 . However, the complexity and variability of mass transport processes have limited the tools available for consistently quantifying geometry in this region. As another example, the transition from curved hilltops to linear hillslopes spans a geometric transition that requires accurate quantification of both slope and curvature with changing surface orientation (Roering et al., 1999b). As digital elevation models (DEMs) become increasingly high resolution in space and multi-temporal (Crosby et al., 2020), there ~~is increasing opportunity to understand landscape development holistically through the development of~~ are growing opportunities to understand landscapes holistically using quantitative tools that are accurate~~across all field settings and can resolve the details of such transitions.~~ , and informative, across all regions of the landscape.

~~However, common topographic analysis workflows use simplistic approaches to DEM analysis that do not extract the full richness of information contained in DEM data, and which introduce known systematic projection error that scales with both slope and curvature (Minár et al., 2020; Bergbauer and Pollard, 2003).~~ The potential of differential geometry for ~~improved~~ DEM processing has already been established in several parallel earth science ~~fields, having been used to calculate~~ disciplines. Examples include models of topographic stresses relevant to critical zone processes (Moon et al., 2017), ~~model mechanisms~~ of sheet joint development on bedrock surfaces (Martel, 2011), and models that describe the structure of bedrock folds (Mynatt et al., 2007; Pearce et al., 2006). ~~Recently, topographic~~ Topographic contour curvature has also been recognized as a key

ingredient for ~~gridscale-independent~~ scale-independent computation of flow accumulation and its role in landscape evolution models (Bonetti et al., 2018, 2020). However, widespread adoption of these techniques has been slow, perhaps because of a conceptual disconnect between resultant metrics of topographic geometry and area-space landscape partitioning frameworks that are at the core of landscape evolution theory.

With this in mind, here we develop a landscape classification workflow based on invariants of the curvature tensor~~that both removes known sources of systematic error in common curvature calculation methods (Minár et al., 2020) and~~ . This provides a fully self-consistent means of calculating all common topographic metrics ~~across process domains in~~ on discretely sampled DEMs ~~.~~ and extracts surface curvature information with rich potential. This approach is robust against distortions that arise from derivative calculations on steep, complex surfaces (Bergbauer and Pollard, 2003; Minár et al., 2020), thus allowing for a curvature-based landscape partitioning approach that is continuous across all process transitions in a fluvial basin. We apply our method to ~~fluvial~~ topography of the Oregon Coast Range, long taken to be a type setting for near-steady-state ~~topography~~ landscape dynamics in which uplift is balanced by erosion ~~everywhere. In addition to the practical benefits of accuracy and reproducibility in computing curvature from DEMs, we demonstrate that this method provides insight into systematic geomorphic process transitions that shape landscapes from hilltops to channel networks~~in locations with characteristic ridge/valley topography.

1.1 ~~Historical context~~The use of curvature in geomorphology

The connection between surface process rates and ~~geometry~~ curvature was recognized as early as the late 19th century when work by G.K. Gilbert and W.M. Davis suggested connections between hillslope convexity and rates ~~and styles of~~ denudation in mountain terrains (Gilbert, 1877; Davis, 1892). ~~Subsequent work (Gilbert, 1908; Fenneman, 1908) showed that both slope and curvature near drainage divides varies systematically with erosion rate and noted that spatial partitioning of dominant erosion mechanisms results in regular geometric patterns toward which landscapes tend to evolve.~~

Efforts to define ~~structures in topography~~ topographic structure predate these observations, however. As has been pointed out in Bonetti et al. (2018), topographic curvature as been studied since at least the middle nineteenth century: Arthur Cayley (Cayley, 1859) used topographic contours to show that watershed bounding ridges are composed of "summits" (we will term these structures "domes") connected by "knots" (we will call these "saddles") such that each ridge line contains one more "summit" than "knot". He argued that "immits" (we will call these "basins") would be similarly connected by bridging saddle structures such that there is one more "immit" than connecting saddle. Prominent physicist James Clerk Maxwell (Maxwell, 1870) ~~then~~ similarly argued that the Earth's surface could be ~~classified as one of~~ sorted into four shape classes; "hills" (domes), "dales" (basins), "passes" connecting hills (antiformal saddles), and "bars" connecting dales (synformal saddles). Maxwell showed that continuity of the surface requires there to always be one more dale than bar, and one more hill than pass, thus reaching the same conclusion as Cayley ~~about the organization of topography without being restricted to ridges and channels.~~

~~We will show that a classification of topographic geometry as a function of upstream drainage area at a point, which is understood to reflect both deep landscape organization (Hack et al., 1957) and geomorphic process regimes (Flint, 1974; Montgomery and~~

~~, provides a quantitative connection between the early landscape organization theories of Maxwell and Cayley and area-space analysis methods common in fluvial geomorphology~~and making a quantitative statement about the distribution of topographic curvatures.

1.2 ~~The use of curvature in geomorphology~~

~~Topographic curvature is~~ Today, several curvature-based metrics are used in geomorphology for surface classification and as an ingredient ~~to~~ in mechanistic transport laws. For examples of classification, Shary (1995) derived 12 curvature metrics which were used in a landscape partitioning scheme, and Passalacqua et al. (2010) used geodesic curvature of topographic contours in combination with drainage area thresholding to extract channel networks from ~~gridded Digital Elevation Models (DEMs),~~ DEMS. Bonetti et al. (2018) showed that curvature is intimately connected to ~~the computation of upstream area~~accumulation of overland flow, Minár et al. (2020) presented an extensive list of possible land surface curvature metrics and proposed possible links to topographic equilibrium, and Schmidt et al. (2003) derived curvature metrics using 2-d polynomial fits of topography for GIS applications. Such classification schemes have proven useful in surface process studies (Sofia, 2020) and for mapping topographic characteristics of hazard susceptibility (Luu et al., 2024) and land use (Riza et al., 2022).

In mechanistic erosion models curvature arises from continuity requirements as the divergence of a gradient driven sediment flux law ~~(Fernandes and Dietrich, 1997)~~(Culling, 1960; **?**). Curvature is thus often used as a quantitative proxy for spatial variation in erosion rates (Struble et al., 2024). For example, at the scale of orogenic provinces, simple models of landscape ~~relaxation in~~ response to uplift ~~use versions of the~~ model erosion with a heat equation where erosion rates are taken to be the product of long-wavelength surface curvature and an empirical diffusivity constant (Watts, 2001; Ruh, 2020). ~~More detailed landscape evolution studies often leverage advection-diffusion equations where sediment transport within fluvial networks (Whipple and Tucker, 1999) is matched by~~ At finer spatial scales, curvature-driven diffusion of ridges ~~and hillslopes (Roering et al., 1999a; O'Hara et al., 2019). Adding~~ (Roering et al., 1999b; O'Hara et al., 2019) is overtaken by advective transport of sediment by concentrated overland flow within the fluvial network as drainage area increases (Whipple and Tucker, 1999), and channels themselves are defined on the basis of curvature (Passalacqua et al., 2010). Accounting for both of these processes and adding a source term to represent bedrock uplift, a commonly used form of the landscape evolution equation arises as

$$\frac{dz}{dt}\frac{\partial z}{\partial t} = U - KA^m|\nabla z|^n - D\nabla^2 z, \tag{1}$$

where z is surface elevation, U is uplift rate, A is drainage area upstream of a given point (a proxy for stream discharge), and K, m, n, and D are empirical constants that account for the geologic, hydrologic, and environmental factors that modulate rates of mass transport. The second term on the RHS is the 'stream power' model for ~~bedrock~~ fluvial erosion (Whipple and Tucker, 1999), while the third term models linear hillslope diffusion. Steady state refers to the situation where $dz/dt = 0$, in which case equation 1 can be rewritten as

$$U = KA^m|\nabla z|^n + D\nabla^2 z. \quad (2)$$

~~Here uplift rate (U) is equal to the sum of the advection of material by the river network and hillslope diffusion, which dominates in unchannelized portions of the landscapes (hillslopes). If the coefficients in equation 2 (U, K, m, n, D; A is always a nonlinear function of spatial position) do not vary spatially or temporally~~ If the parameters K, m, n, and D in Eq. 2 are spatially and temporally constant, then variation in ~~stream~~ the geometric properties of a topographic surface (such as stream longitudinal gradient and hilltop curvature~~map~~) maps variation in uplift rate U (Wobus et al., 2006). Conversely, in regions where uplift is ~~spatially uniform, variation in these coefficients~~ uniform, geometric variation can be used to infer the effects of climatic, lithologic, and environmental factors on the rate and style of erosion (Ferrier et al., 2013; Stock and Montgomery, 1999; Amundson et al., 2015).

An extensive literature has been established leveraging one or both of these limits (Perron et al., 2009; Whipple et al., 2013). ~~However, the utility and reproducibility of this approach depends on accurate calculation from DEMs of curvature, slope, and upstream catchment area~~

We show that a formal differential geometry approach extracts geometric information from the curvature tensor directly, and can provide a self-consistent means of evaluating topographic form across process domains. Comparing invariants of the curvature tensor to upstream drainage area A at a point, a quantity assumed to underlie empirical scaling relations (Hack et al., 1957) and process regimes (Flint, 1974; Montgomery and Buffington, 1997; Kirby and Whipple, 2012) alike, provides an intuitive description of river basin development. This approach also makes a quantitative connection between the early landscape organization theories of Maxwell and Cayley and drainage area analysis methods common in fluvial geomorphology today.

2 Oregon Coast Range study site

We test our method of geometric classification in the central Coast Range, USA, a forearc landscape of the Cascades subduction zone. Our study area is a suite of ~ 10 km^2 basins that host fluvial and debris flow channel networks between the Umpqua and Smith River basins near Reedsport, Oregon. Bedrock in this study area is composed entirely of the Tyee Formation (Baldwin, 1961; Beaulieu and Hughes, 1975), a 3 km thick suite of accreted Eocene turbidites that was subject to uplift during the Miocene (McNeill et al., 2000; Wells et al., 2014) and continues to be uplifted today with long-term rates ranging from 0.05 mm yr^{-1} to over 0.4 mm yr^{-1} (Kelsey et al., 1996; Personius, 1995).

The Coast Range has long been identified and studied as an archetypal steady-state landscape due to its uniform ridge-valley topography (Dietrich and Dunne, 1978; Montgomery, 2001), and documented correlations between ~~catchment~~ drainage averaged erosion rates, uplift rates, and topographic proxies for erosion rate (Reneau and Dietrich, 1991; Heimsath et al., 2001; Struble et al., 2024). We focus on a small portion of the Coast Range ~~where we do not expect to see the~~ without much variation in lithology (Baldwin, 1961; Beaulieu and Hughes, 1975) or climate (Daly and Bryant, 2013). Owing to the relatively gentle

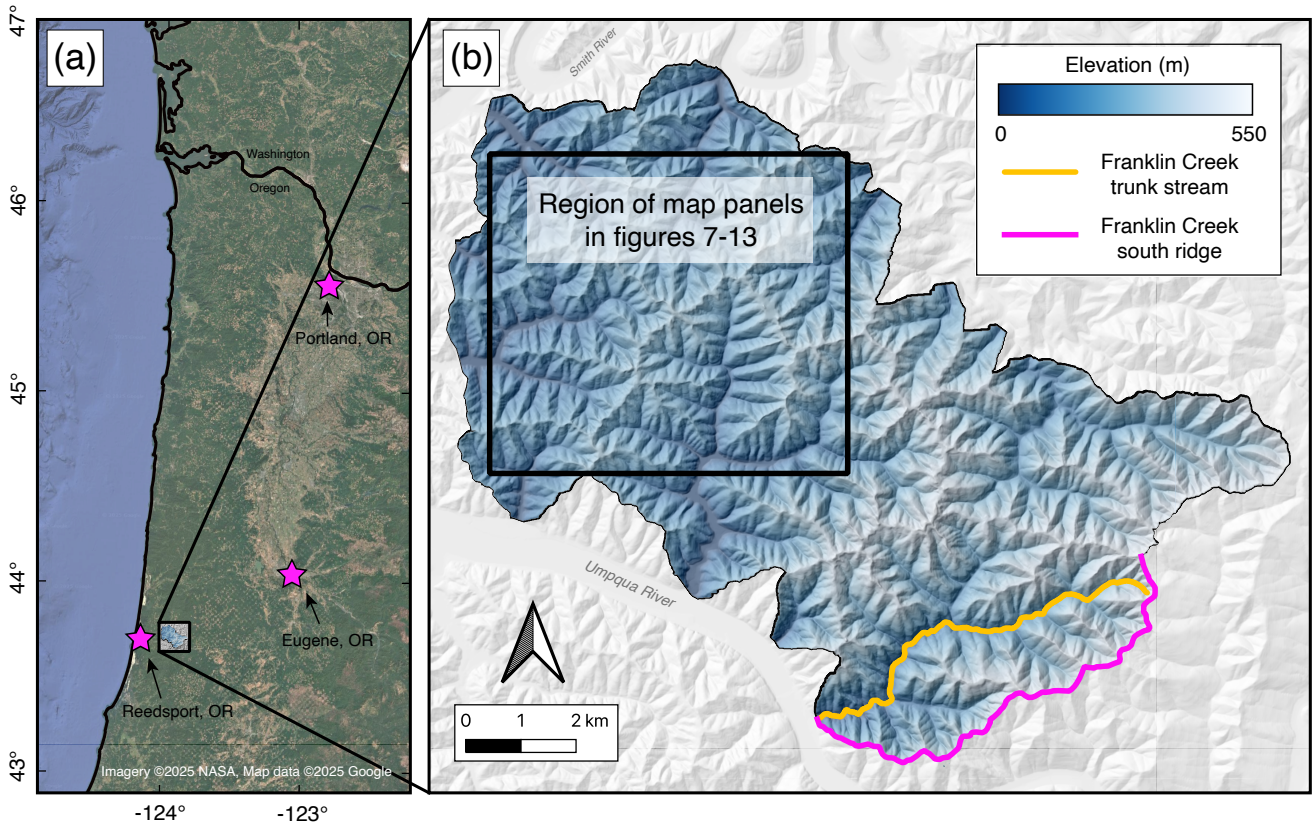

Figure 1. **Map of study area. a.** Overview map of Cascadia coastal region showing location of study site. Satellite imagery from Google Earth, accessed through QGIS XYZ tiles on June 13th, 2025. **b.** Elevation map of study area showing location of the Franklin Creek trunk stream and southern ridge of Franklin Creek basin analyzed in Sect. 5.3. Black outline shows region of focused maps in figures 7-13

dip of the bedrock, this area is not subject to deep-seated landslides that interrupt characteristic ridge-valley terrain in other portions of the Coast Range (Roering et al., 2005; LaHusen et al., 2020).

~~Map of study area. a.Overview map of Cascadia coastal region showing location of study site. Satellite imagery from Google Earth, accessed through QGIS XYZ tiles on June 13th, 2025. b.Elevation map of study area showing location of the Franklin Creek trunk stream and southern ridge of Franklin Creek basin analyzed in section 5.3. Black outline shows region of focused maps in figures 7-13~~

3 Definitions of curvature

4 ~~Intrinsic versus extrinsic topographic curvature~~

3.1 Intrinsic versus extrinsic curvatures

The term "curvature" formally refers to a class of mathematical operations that ~~describe the degree to which~~ quantify deviations of a surface (or more generally, a manifold) ~~deviates~~ from being planar (Needham, 2021). The tools of differential geometry and tensor calculus were in part developed to describe these operations ~~. Measures of curvature~~(Pesic, 2007). There are several ways to define curvature, which can be classified as either 'intrinsic' or 'extrinsic'~~where intrinsic curvatures are invariant qualities of a surface, meaning their value is independent of external coordinate systems~~. Intrinsic curvatures are independent of coordinate system and can be calculated using only local surface information (Needham, 2021). ~~Conversely, extrinsic measures~~ Extrinsic curvatures are built using external coordinates and so ~~their values depend on orientation of a surface within a given reference frame (Struik, 1950; O'Neill, 2006; Minár et al., 2020)~~depend on the choice of reference frame (Struik, 1950; O'Neill, 2006).

~~Many topographic analysis workflows calculate curvature as an extrinsic scalar quantity given by the Laplacian $\nabla^2 z(x,y)$ where z is elevation, ∇ is the gradient operator, and the reference frame is given by east-west coordinates of DEM pixels. Usually this quantity is either calculated directly from gridded DEMs or polynomial fits of elevation data (Hurst et al., 2012a; Schmidt et al. . While the Laplacian gives a curvature value proportional to the intrinsically defined mean Curvature (Sect. 3.2), these approaches admit systematic slope-dependent error (Bergbauer and Pollard, 2003; Minár et al., 2020) in addition to error that stems from~~ On discretely sampled landscape models (DEMs), the accurate calculation of either intrinsic or extrinsic curvatures requires careful consideration of coordinates to avoid distortions that come from projection of topography onto a ~~regularly sampled 2-d grid. Instead a DEM is must be viewed as a set of irregularly spaced data points sampling a 2-d surface embedded in a 3-dimensional space. This distinction is important because, while map-view projections of DEMs assume uniform distances and angles between grid points, lines on a topographic surface change length and orientation with changing curvature and slope resulting in a breakdown of euclidean assumptions on which the Laplacian method is based (Needham, 2021).~~

map grid. The effects of ~~the projection process~~ projection can be seen in Fig. 2, which compares the distances and angles of a map projection (Fig. 2.a) to those of the same grid lines ~~overlain on a 3-d representation of the~~ overlaying the 3-D surface (Fig. 2.~~a). We see that the~~ b). In the map-view representation, the E-W and N-S grid lines ~~in Fig. 2.a) are not perpendicular on the surface Fig. 2.b) and change orientation between grid nodes. As a result grid cells do not have uniform dimensions and can not be described with a universal coordinate system. One way to visualize this is to imagine walking~~ are perpendicular and evenly spaced. If one were to define displacement vectors $\mathbf{dx}$ and $\mathbf{dy}$ emanating from point p along ~~displacement vectors defined by the map-view grid lines. In the map view projection it is clear that one would arrive at point $\hat{q}$ located a distance $d\hat{s}$ from the origin, howeverin fact one would travel the distance ds arriving at point~~ these grid lines, their combination would create a resultant displacement $\mathbf{d\hat{s}}$ ending at point $\hat{\mathbf{q}}$. In Fig. 2.b, however, displacement vectors $\mathbf{du}$ and $\mathbf{dv}$, which connect p to the same points on the surface as $\mathbf{dx}$ and $\mathbf{dy}$ respectively, are not perpendicular and their combination results in a displacement

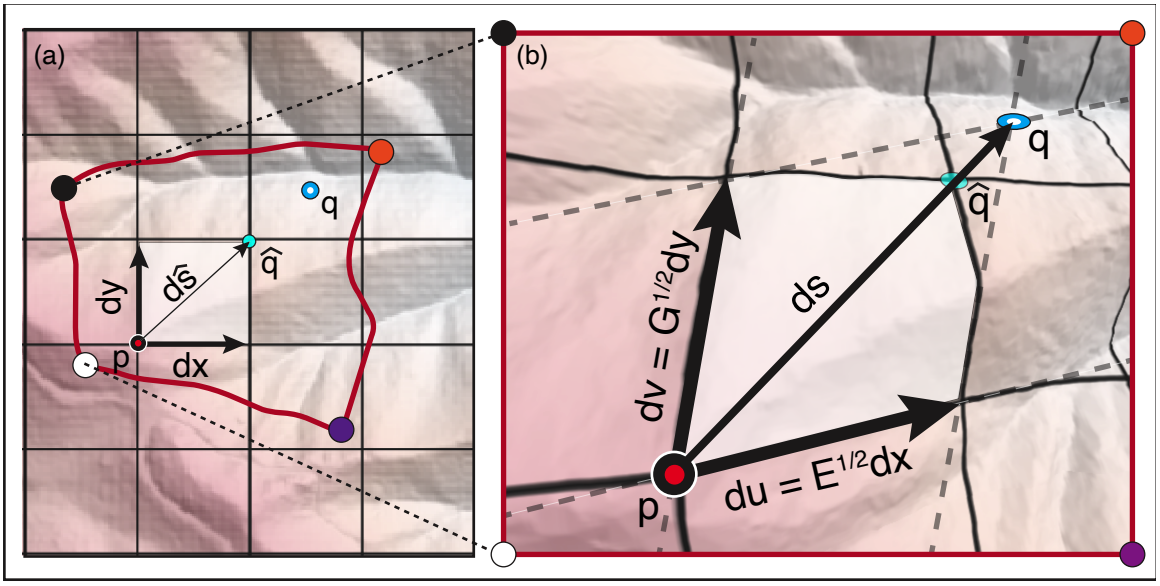

Figure 2. Difference between distances and angles measured on a map projection versus on the surface. a. Map projection of DEM including map grid defined by E-W and N-S lines with grid spacing dx and dy. The red line corresponds to the rectangular outline of panel b. **b.** DEM viewed as a 2-d manifold embedded in a 3-d space. Dashed lines ~~how~~ show a locally defined ~~u-v~~ uv coordinate system that follows x and y curves on the map projection, but which are not orthogonal or of equal length due to surface distortion. E and G are coefficients of the first fundamental form, and ds is the displacement vector that results moving one grid space along each of these coordinate vectors

(ds) that maps to a different point (q~~. The effects of this distortion on the accuracy of curvature, slope, and drainage area calculations will be explored quantitatively in section 6.~~). It can be seen that neighboring grid cells do not have uniform dimensions, and that the angle between the grid lines is not consistent.

~~The problem of projection error for topographic maps~~ Thus, accurate geometric calculations on topography require viewing a DEM not as a regular grid, but as a set of irregularly spaced data points sampling a surface, an approach that is similar in spirit to how elevation data are treated in landscape evolution models (Tucker et al., 2001). To accurately define a surface, distances and angles between grid cells are not treated as uniform quantities, as they result from calculations of surface variation about each point in a local reference frame. This specific problem of topographic projection was recognized by Leonard Euler in 1775 and motivated the work of Carl Frederick Gauss, who, roughly fifty years after Euler's observation, established the ~~modern method for calculating the curvature~~ mathematical framework for accurate geometric classification of surfaces (Gauss, 1902; Needham, 2021). ~~Gauss recognized that, while Euclidean spaces exhibit global parallelism (parallel lines remain parallel forever; Fig.2.a) curved surfaces do not. Gauss addressed this by defining a locale, non-orthogonal, coordinate system at each point (the dashed lines in Fig. 2.b for point p) and discovered he could characterize local variations in the surface via the coefficients of two quadratic equations known as the first and second fundamental forms. This discovery paved the way for the fundamental theorem of surface theory, proved in 1867 by Pierre Ossian Bonnet (Cogliati and Rivis, 2022). This theorem~~

~~states that all qualities of a surface, with the exception of its orientation in space, can be derived using the 6 coefficients of the first and second fundamental forms.~~

~~During the same time period Bernhard Riemann, a student of Gauss, set the stage for modern differential geometry by generalizing Gauss' ideas to higher dimensional spaces and showing that characterizing curvature of an n-dimensional manifold requires $\frac{1}{12}n^2(n^2-1)$ distinct coefficients (Pesic, 2007). Thus while a single measure of curvature (e.g. the Laplacian)is sufficient to characterize a 2-d map projection of topography, accurate representation of 3-d topography requires six distinct components; the coefficients of the first and second fundamental forms. It is worth noting that most modern treatments of curvature~~ Using an approach similar to Gauss, ~~including profound discoveries in physics of the 20th century (e.g. general relativity; Einstein and Lawson (2013)) , use the tools of tensor calculus for which these six coefficients are the independent components of the 'Riemannian curvature tensor' Needham (2021). However, the original theory is sufficient for our analysis of topography, so we use Gauss' classical definition of~~ we derive both intrinsic and extrinsic topographic topographic curvature metrics built on invariant surface quantities.

3.2 Curvature invariants and related shape classes categories

As you change orientation about any point on a continuous surface, two perpendicular directions define the maximum and minimum normal curvature values (Needham, 2021). Between these directions, the curvature varies smoothly as

$$\kappa(\theta) = k_1 \cos^2\theta + k_2 \sin^2\theta, \tag{3}$$

where the extrema k_1 and k_2 are called the principal curvatures and θ is an angular direction measured within the surface ~~curvature here.~~ tangent plane. Equation 3, known as Euler's Theorem (not to be confused with the 'Euler's Theorem' in number theory or the 'Euler Identity' of complex analysis), shows that the principal curvatures can be used to calculate normal curvature along any path over the surface. The principal curvatures are invariant quantities, meaning their values are independent of reference frame.

4 ~~Spectral filtering of gridded datasets~~

~~In order to calculate the curvatures of DEMs it is necessary to do some degree of smoothing to both remove artifacts of the gridding process (Reuter et al., 2009; Bui and Glennie, 2023; Bater and Coops, 2009) and generate a mathematically continuous surface that satisfies the differentiability requirement of calculus (Stewart, 2003). For this study we select 8.1 mresolution DEM data freely available through the National Map (https://apps.nationalmap.gov/downloader/). While higher resolution LiDAR (Light Detection and Ranging) data are available in the study area we select the courser dataset, which gives substantially shorter computation times while still resolving geometric trends at the scale of fluvial basins.~~ The principal curvature can be used to calculate two other useful invariant quantities that will be more central to our analysis; the 'mean' and 'Gaussian'

curvatures. The mean curvature, and extrinsic quantity, follows directly from Euler's Theorem and is the value about which the curvature oscillates as a function of angle on the surface (Eq. 3). While it can be calculated as the average curvature of any two perpendicular paths, we define it in terms of the principal curvatures as

$$K_M = \frac{k_1 + k_2}{2}. \tag{4}$$

~~Numerous tools are available for smoothing digital topographic data, including b-spline fitting (Brigham and Crider, 2022), wavelets (Struble et al., 2024), selective denoising (Gallant, 2011), and TIN inerpolation (Jordan, 2007). We choose to filter the data using a Discrete Fourier Transform (DFT; also a contribution of Gauss (Heideman et al., 1985)), which decomposes discretely sampled signals into sums of harmonic functions. Smoothing is accomplished via low-pass filter, where information at wavelengths smaller than a defined cutoff is removed. Fourier methods have been extensively applied in geomorphology including the identification of characteristic process scales (Perron et al., 2008), landform identification (Booth et al., 2009), and to assess topographic controls on mass transport mechanics (Richardson and Karlstrom, 2019; Black et al., 2017; Crozier et al., 2018) .~~

~~One challenge of Fourier methods in topographic analysis is that harmonic functions do not naturally respect the finite nature of a DEM in which boundaries are non-homogeneous. Tapering of the data is thus required to obtain zero elevation at the boundaries prior to DFT. It is common to accomplish this by convolving the DEM grid with a 2-d raised cosine (aka Hanning window), such that the resulting topography is equal to its actual value only in center of the grid, and is elsewhere subdued by an amount that scales with distance towards the margins (Perron et al., 2008). A downside of this approach is that it diminishes the spectral power of relevant landscape features, and introduces artificial long-wavelength signals that are difficult to differentiate from real structures in the resulting power spectrum.~~

~~Fortunately, solutions can be found (Harris, 1978; Kirby, 2014) . For example Menutt (1983) showed that spectral contamination can be minimized by first reflecting the topographic grid along each coordinate axis, then tapering the data only in~~ The Gaussian curvature (K_G) can be defined as the product of the ~~reflected portions that fall outside the limits of the original DEM. This avoids the introduction of distortion within the study area through the windowing process, and only introduces artificial signals with significant power that are at or above the scale of the full DEM extent.~~ principal curvatures

$$K_G = k_1 k_2. \tag{5}$$

This value is intrinsic, meaning both that it is unchanged under isometric transformations, and that it does not depend on the actual shape of the surface in space. Instead K_G captures a more subtle quality: the degree of stretching or bending required to deform a flat plane so that it conforms to the surface (O'Neill, 2006). Note that the units of K_G (m^{-2}) are not the same as K_M (m^{-1}).

~~We adopt this mirroring approach and apply a Tukey window, which consists of a boxcar function convolved with a cosine taper along the margins (Harris, 1978). We apply the default Tukey window in the *window2* function in Matlab and find that this~~

~~method minimizes the introduction of spurious signals in the pre-processing step~~The mean and Gaussian curvatures together determine the geometry about a point uniquely as one of eight distinct shape classes (Bergbauer and Pollard (2003); Fig. 3).

~~The Discrete Fourier Transform (DFT) is calculated as~~

$$Z(k_x, k_y) = \sum_{p=0}^{N_x-1} \sum_{q=0}^{N_y-1} z(p\Delta x, q\Delta y) e^{-2\pi i(\frac{k_x p}{N_x} + \frac{k_y q}{N_y})}$$

~~where N_x and N_y are~~ Since the Gaussian curvature is the ~~number of grid cells in each direction, p~~ product of the two principal curvatures, it will only be positive in instances where k_1 and ~~q are array indices, Δx~~ k_2 have the same sign. Positive K_G thus correlates to either domes or basins, though we cannot discern which from K_G alone. If K_G is negative, then k_1 and ~~Δy are the grid spacings in each direction, and k_x and k_y are the wavenumbers in the respective x and y directions (Perron et al., 2008). Each value in the output array given by the above equation is associated with a frequency in x and y directions with magnitudes~~

$$f_x = \frac{k_x}{N_x \Delta x}, \qquad f_y = \frac{k_y}{N_y \Delta y}.$$

~~These frequencies can then be used to define a radial frequency as~~

$$f_r = \sqrt{(f_x^2 + f_y^2)}.$$

~~The DFT periodogram is then given by~~

$$P_f(k_x, k_y) = \frac{1}{N_x^2 N_y^2} |Z(k_x, k_y)|^2$$

k_2 have opposing signs and the surface is locally a saddle. Again, the orientation in space cannot be determined from this intrinsic quality.

~~Following Perron et al. (2008) we design a half-Gaussian filter based on radial frequencies defined as~~ In cases where either k_1 or k_2 is equal to zero, K_G is also zero. Such shapes comprise a class of 'developable surfaces', which are intrinsically flat and can be formed from a plane without altering surface area (Needham, 2021). 'Relatively developable surfaces' can be extracted from the landscape by assigning a zero value to curvatures under a defined threshold (Mynatt et al., 2007). Curvature thresholding to extract developable forms is a promising approach for classifying landforms. However, we do not explore this further here.

$$F_{low} = \begin{cases} 1, & f < f_1 \\ \exp\left(\frac{-(f-f_1)^2}{2\sigma^2}\right), & f \geq f_1 \end{cases}$$

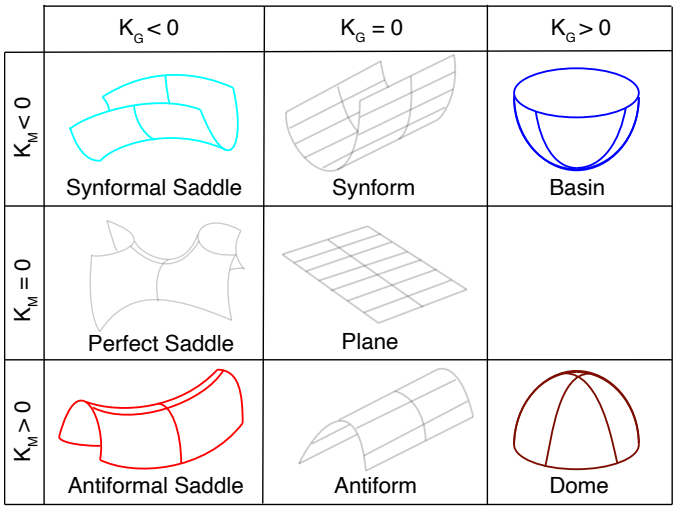

Figure 3. Shape classes into which points on the surface can be sorted based on the signs on the Mean (K_M) and Gaussian (K_G) curvatures. In this analysis we focus on those classes that can be assigned based on raw curvature values, which are synformal saddles, antiformal saddles, basins, and domes, and do not include developable surfaces or perfect saddles. Modified from Mynatt et al. (2007)

~~where $\sigma = \frac{1}{3}|f_2 - f_1|$ is the standard deviation. The filter is convolved with the radial frequency spectrum to suppress frequencies outside the filter tapering window. The filtered spectrum is then reversed transformed, and~~ The orientation of a shape is an extrinsic quality that can be determined from the mean curvature, allowing us to put geometric classifications based on K_G into a landscape reference frame. K_M is positive in two cases: when both k_1 and k_2 are positive, or when the higher-magnitude curvature (k_1) is positive. This means that points in the landscape with $K_M > 0$ are concave down and are locally either domes or antiformal saddles. Similarly, if K_M is negative, then the surface must be mostly concave up and is either a basin or synformal saddle. More generally, the sign of the ~~original domain of the DEM is extracted from the windowed representation to yield a low-pass filtered raster of topography~~mean curvature allows us to differentiate between the divergence and convergence of surface gradient vectors.

4 ~~Calculation of curvature~~

~~In this section we derive the coefficients of Gauss' two fundamental forms, and use them to calculate curvature metrics used in our topographic analysis. While there are several methods for deriving these quantities, we base our derivation on that of Struik (1950) (Chapter 2). See also Bergbauer and Pollard (2003), Mynatt et al. (2007), and Martel (2011) for similar geologically motivated derivations. Note that we use prime notation for partial derivatives relative to directions given by subscript indices ($\mathbf{r}'_u = \partial \mathbf{r}/\partial u$).~~ In cases where k_1 and k_2 are equal and opposite the surface is a perfect saddle. This too comprises its own special class of surfaces, known as 'minimal surfaces', which have arisen in models for optimization of surface area in self-organizing systems such as soap foams, cell membranes, and crystal lattices (Osserman, 2013). The

existence of approximate perfect saddles could be explored in a geomorphologic context by assigning a threshold below which curvature variation is assumed negligible. Again, we do not endeavor to explore this here, instead focusing on the 4 basic shape classes that can be assigned based on raw curvature calculations. This will provide us with sufficient information to quantify patterns in landscape curvature, and relate these to the evolution of geomorphic process regimes with upstream drainage area.

3.1 ~~Deriving the first and second fundamental forms~~

~~Surface curvature at a given point can be defined by considering an arbitrary path drawn over the surface . Infinitesimal displacements along such a path trace out arcs that lie within a plane containing the unit tangent ($\mathbf{t}$) and normal ($\mathbf{N}$) vectors of the curve (known as the 'osculating plane'). We define~~

3.1 Finding the principal curvatures

Defining curvature rigorously on discretely sampled topography requires accounting for changes in surface orientation between neighboring points, and how that change is scaled by non-uniform distances on a complicated surface. Our derivation of principal curvatures largely follows Struik (1950), though we will point to complementary references throughout. First, a position on the surface is taken to be the endpoint of a position vector ~~to a point on the surface in 3-d cartesian space as~~ parameterized by uv-coordinates such as those shown in Fig. 2.b, but referenced to a Cartesian basis via as

$$r=r\mathbf{r}(u,v) = r_1\mathbf{e}_1{}_1\hat{\mathbf{e_1}} + r_2\mathbf{e_2}_2\hat{\mathbf{e_2}} + r_3\mathbf{e_3}_3\hat{\mathbf{e_3}} \tag{6}$$

where the ~~parameters~~ $\hat{\mathbf{e}}_\mathbf{i}$ are unit vectors corresponding to easting, northing, and elevation, and u and v ~~represent~~ are coordinates following any two intersecting curves on the surface~~that define a local coordinate system, and $\mathbf{e_1}$, $\mathbf{e_2}$, and $\mathbf{e_3}$ are Cartesian basis vectors. The choice of u and v is completely arbitrary except for the requirement~~

$$\mathbf{r}'_u \times \mathbf{r}'_v \neq 0$$

~~which ensures that a normal vector can be defined. In our case the the u and v curves follow the E-W and N-S DEM grid lines .~~

~~For any small displacement (ds) a tangent vector ($\mathbf{t}$) and unit normal vector ($\mathbf{N}$) can be defined in terms of the u, v curves as~~

$$\mathbf{t}= d\mathbf{r}/ds$$

~~and~~

$$\mathbf{N}= \frac{\mathbf{r}'_u \times \mathbf{r}'_v}{|\mathbf{r}'_u \times \mathbf{r}'_v|}.$$

~~respectively, where $d\mathbf{r} = \mathbf{r}'_u du + \mathbf{r}'_v dv$ is the change in position resultant of a small displacement~~ In this case the uv-coordinates follow the lines on the map-view grid, but we do not assume orthogonality on the surface. ~~Equation ?? is the unit normal of the tangent plane ($\mathbf{N} = N_1\mathbf{e_1} + N_2\mathbf{e_2} + N_3\mathbf{e_3}$) with the slope of the tangent plane given by~~

$$S_T = \left|\tan\left(\frac{\pi}{2} - \sin^{-1}(N_3)\right)\right|.$$

~~The magnitude of a displacement along the curve is given by the Pythagorean Theorem as~~ The square of the infinitesimal arc-length between points is then given by

$$I = ds^2 = d\mathbf{r} \cdot d\mathbf{r} = Edu^2 + 2Fdudv + Gdv^2. \tag{7}$$

~~Equation ?? is Gauss' first fundamental form (I), also called the surface metric formula. It is a measure of distances on the surface, where $E = \mathbf{r}'_u \cdot \mathbf{r}'_u$, $F = \mathbf{r}'_u \cdot \mathbf{r}'_v$, and $G = \mathbf{r}'_v \cdot \mathbf{r}'_v$~~ where $E = \frac{\partial \mathbf{r}}{\partial u} \cdot \frac{\partial \mathbf{r}}{\partial u}$, $F = \frac{\partial \mathbf{r}}{\partial u} \cdot \frac{\partial \mathbf{r}}{\partial v}$, and $G = \frac{\partial \mathbf{r}}{\partial v} \cdot \frac{\partial \mathbf{r}}{\partial v}$ (the metric coefficients) quantify the proportionality of distances measured on the surface to distances in the ~~projected cartesian reference frame(Needham, 2021). The metric coefficients also allow us~~ Cartesian reference frame. They can also be used to calculate the ratio of ~~surface area on topography to the~~ area ~~of a grid cell via the relation~~

$$\alpha = \sqrt{EG - F^2}.$$

~~We will use this 'area expansion factor' (α) to compare intrinsic versus extrinsically derived drainage area in section 6. Along any surface curve ds that locally follows the shortest path between points (geodesic)~~on the ~~only curvature will be the 'normal curvature' (κ) which measures rotation of the surface tangent along the curve. Mathematically this can be defined~~ surface to pixel area as ~~the projection of the full derivative of the unit tangent onto the unit normal written~~

$$\frac{d\mathbf{t}}{ds} = \left(\frac{d\mathbf{t}}{ds} \cdot \mathbf{N}\right)\mathbf{N} = \kappa\mathbf{N}.$$

$\alpha = \sqrt{EG - F}$, a quantity we will use to calculate intrinsic drainage areas in our analysis (Sect. 4).

Equation 7, known as the first fundamental form or surface metric formula, allows us to accurately calculate distances and areas on the surface. This in turn can be used to scale topographic curvatures. Curvatures are calculated as a change in surface orientation along a path, defined as

$$II = d\mathbf{r} \cdot \mathbf{N} = edu^2 + 2fdudv + gdv^2, \tag{8}$$

~~It follows that the normal curvature is~~

$$\kappa = \frac{d\mathbf{t}}{ds} \cdot \mathbf{N} = -\mathbf{t} \cdot \frac{d\mathbf{N}}{ds}$$

where ~~$d\mathbf{N} = \mathbf{N}'_u du + \mathbf{N}'_v dv$. Plugging in equation ?? as the definition of the tangent vector , equation ?? can be rewritten as~~ $e = \frac{\partial^2 \mathbf{r}}{\partial u^2} \cdot \mathbf{N}$, $f = \frac{\partial^2 \mathbf{r}}{\partial u \partial v} \cdot \mathbf{N}$ and $g = \frac{\partial^2 \mathbf{r}}{\partial v^2} \cdot \mathbf{N}$ (the curvature coefficients) are the projection of directional curvatures onto a unit normal vector

$$\kappa\mathbf{N} = -\frac{d\mathbf{r}}{ds} \cdot \frac{d\mathbf{N}}{ds} = -\frac{edu^2 + 2fdudv + gdv^2}{Edu^2 + 2Fdudv + Gdv^2} = -\frac{II}{I} \frac{\frac{\partial \mathbf{r}}{\partial u} \times \frac{\partial \mathbf{r}}{\partial v}}{\left|\frac{\partial \mathbf{r}}{\partial u} \times \frac{\partial \mathbf{r}}{\partial v}\right|}. \tag{9}$$

~~The expression in the numerator~~

$II = d\mathbf{r} \cdot d\mathbf{N} = edu^2 + 2fdudv + gdv^2$

~~is~~

Equation 8 is called the second fundamental form~~(II) with coefficients $e = \mathbf{r}''_{uu} \cdot \mathbf{N}$, $f = \mathbf{r}''_{uv} \cdot \mathbf{N}$, and $g = \mathbf{r}''_{vv} \cdot \mathbf{N}$ that measure~~ , and measures changes in the orientation of the tangent plane along ds. Combining the information in Eqs. 7 and 8 as

$$\kappa = -\frac{II}{I} = -\frac{d\mathbf{r}}{ds} \cdot \frac{d\mathbf{N}}{ds} = -\frac{edu^2 + 2fdudv + gdv^2}{Edu^2 + 2Fdudv + Gdv^2} \tag{10}$$

~~Equation 10~~ allows us to completely define the shape of a ~~complicated~~ surface in 3-d space~~using a cartesian coordinate system~~ . Resultant curvature values reference the Cartesian coordinate system given by the map grid, but without the assumption of orthogonality on the surface that ~~leads to systematic error in the Laplacian~~otherwise leads to projection distortion. The coefficients of the second fundamental form (e, f and g; ~~Equation ??~~eq. 8) are the directional curvatures where e and g correspond to curvature along the E-W and N-S grid line respectively, and f is a cross term that accounts for ~~the lack of orthogonality of these directions on the surface. These curvatures~~ directional covariance. These values are scaled by the coefficients of the first fundamental form (E, F, and G; ~~Equation ??~~eq.7), which maps lengths on the coordinate grid to lengths on the surface accounting for the effect of slope on surface distances~~and areas. Together these six coefficients allow for the rigorous classification of topographic surfaces that meets criteria set forth by the fundamental theorem of surface theory, and allows us to compute topographic curvatures in a way that minimizes known distortion inherent in extrinsic surface classification methods.~~ .

3.2 ~~Finding the principal curvatures~~

~~Equation 10 is a general expression for curvature for a single path over the surface. The existence of infinite paths through any given point means there are infinite measures of curvature possible, however there always exist two perpendicular paths along which the maximum and minimum curvatures are found. This observation is attributed to Euler, who showed that as the osculating plane rotates about an axis defined by the surface normal vector $\mathbf{N}$ of a continuous surface the normal curvature (κ; equation 10) varies as~~

$\kappa(\theta) = k_1 \cos^2\theta + k_2 \sin^2\theta,$

where k_1 and k_2 are the extrema, termed the two 'principal curvatures', and θ is angular direction measured within the surface tangent plane. Equation 3, known as Euler's Theorem, shows that once the principal curvatures are known they can then be used to calculate curvature along any path over the surface (not to be confused with the 'Eulers Theorem' in number theory or the 'Euler Identity' of complex analysis). Fig. **??** shows a plot of Equation 3 noting the location of principal curvatures and the Mean Curvature, which will be discussed further in the following section. Curvature as a function of the angle between the osculating plane and a reference direction.Here the angle $\theta = 0$ is associated with the first principal curvature (k_1). k_2 is the second principal curvature and K_M is the Mean curvature about which the value oscillates. To find the directions of the two principal curvatures we first define a new The directions of the principal curvatures can be found algebraically by defining a parameter $\lambda = dv/du$, allowing us to rewrite Equation 10 in terms of a single variable as and rewriting Eq. 10 as

$$\kappa = \frac{edu^2 + 2f\lambda du^2 + g\lambda^2 du^2}{Edu^2 + 2F\lambda du^2 + G\lambda^2 du^2} = \frac{e + 2f\lambda + g\lambda^2}{E + 2F\lambda + G\lambda^2} \frac{e + 2f\lambda + g\lambda^2}{E + 2F\lambda + G\lambda^2}. \tag{11}$$

The Since the principal curvatures correspond to extrema where $d\kappa/d\lambda = 0$, so we differentiate Equation we differentiate eq. 11 with respect to λ and set the result equal to zero giving . The result is given by

$$\frac{d\kappa}{d\lambda} = (E + 2F\lambda + G\lambda^2)(f + g\lambda) - (e + 2f\lambda + g\lambda^2)(F + G\lambda) = 0. \tag{12}$$

Rearranging Equation 12 gives

$$(Fg - Gf)\lambda^2 + (Eg - Ge)\lambda + (Ef - Fe) = 0, \tag{13}$$

a quadratic equation in λ with roots that whose roots correspond to the principal curvature directions. Recalling that $\lambda = dv/du$ we can then convert these principal directions into angles defined equate these values to angles in our local u-v coordinate system uv-coordinate system and can thus reference principal curvature orientations within the map-view grid.

The magnitudes Magnitudes of the principal curvatures can similarly be found by finding a quadratic equation in the parameter of interest, in this case the normal curvature κ. Given the condition be found through a similar approach. Since $d\kappa/d\lambda = 0$ at curvature extrema equations along the principal directions, 11 and 12 can be combined to give a simpler expression for the curvature

$$\kappa = \frac{f + g\lambda}{F + G\lambda}. \tag{14}$$

Recognizing that

$$E + 2F\lambda + G\lambda^2 = (E + F\lambda) + \lambda(F + G\lambda) \tag{15}$$

and

$$e + 2f\lambda + g\lambda^2 = (e + f\lambda) + \lambda(f + g\lambda), \tag{16}$$

~~we show that~~ eq. 12 can be rearranged to show

$$\kappa = \frac{f + g\lambda}{F + G\lambda} = \frac{e + f\lambda}{E + F\lambda}. \tag{17}$$

~~and so we arrive at two equivalent expressions for defining the curvature~~

~~$\kappa = \frac{f + g\lambda}{F + G\lambda} = \frac{e + f\lambda}{E + F\lambda}.$~~

The two expression for curvature given by ~~Equation ??~~ eq. 17 can be rearranged as

$$f - \kappa F + \lambda(g - \kappa G) = 0 \tag{18}$$

and

$$e - \kappa E + f - \kappa F = 0, \tag{19}$$

respectively. ~~If we then multiply both equations through~~ Multiplying eqs. 18 and 19 by du (~~remembering that~~ with $\lambda = dv/du$) ~~then~~ we arrive at a system of ~~equations in terms of our original u-v coordinate~~ linear equations in our original uv-coordinate system

$$\begin{bmatrix} e - \kappa E & f - \kappa F \\ f - \kappa F & g - \kappa G \end{bmatrix} \begin{bmatrix} du \\ dv \end{bmatrix} = \begin{bmatrix} 0 \\ 0 \end{bmatrix}. \tag{20}$$

This has a non-trivial solution only if the determinant of the coefficient matrix is zero~~, which corresponds to~~

~~$(EG - F^2)\kappa^2 - (gE - 2fF + eG)\kappa + (eg - f^2) = 0,$~~

~~a~~. The corresponding quadratic equation in κ ~~. The roots of Equation 21~~

$$(EG - F^2)\kappa^2 - (gE - 2fF + eG)\kappa + (eg - f^2) = 0 \tag{21}$$

has roots that are the principal curvatures~~of the surface. The more positive principal curvature is typically called~~. By convention, we take the more positive of these roots to be k_1, while the less positive curvature is k_2. ~~In this work~~ We also assume that positive curvatures are ~~defined as~~ concave down.

3.2 Justification of the classical approach

It should be noted that ~~in more modern literature the information contained in the fundamental forms is often presented in the Shape Operator, which is the second order tensor given by taking the negative gradient of a normal vector along an arbitrary tangent. This is written mathematically as~~

~~$S(\mathbf{t}) = -\nabla_{\mathbf{t}}\mathbf{N}$~~

~~where $\nabla_{\mathbf{t}}$ is the gradient defined along tangent vector $\mathbf{t}$ (O'Neill, 2006). In terms of our u-v coordinate curves the first and second fundamental forms can be defined via this approach as $I(\mathbf{u},\mathbf{v}) = \mathbf{u} \cdot \mathbf{v}$ and $II(\mathbf{u},\mathbf{v}) = S(\mathbf{u}) \cdot \mathbf{v}$.~~

~~The~~ here we have taken a deliberately classical approach to finding the principal curvatures and related invariants. Modern differential geometry is mostly based on tensor formulations, wherein the information contained in the first fundamental form is ~~used to construct~~ stored in the 'metric tensor'

$$Ig_{ij} = \begin{bmatrix} E & F \\ F & G \end{bmatrix}, \tag{22}$$

~~while~~ and the information of the second fundamental form is stored in the 'surface curvature tensor'

$$IIb_{ij} = \begin{bmatrix} e & f \\ f & g \end{bmatrix}. \tag{23}$$

~~The Shape Operator is then given by~~

$$S = I^{-1}II.$$

Curvature invariants are extracted from the shape operator, a rank-2 tensor given by taking the negative gradient of a normal vector along an arbitrary tangent ($S(\mathbf{t}) = -\nabla_{\mathbf{t}}\mathbf{N}$; O'Neill (2006)), or alternatively as the product of the inverse metric tensor and curvature tensor ($S^i_j = g^{ik}b_{kj}$). The eigenvalues of the ~~Shape Operator~~ shape operator are the principle curvatures, and the eigenvectors define the directions associated with ~~these curvatures~~k_1 and k_2. The Gaussian and ~~Mean curvatures , which we will define in the following section, are the determinate and trace of this matrix~~ mean curvatures are the determinant and half-trace of the shape operator, respectively.

3.3 ~~Mean and Gaussian Curvatures, General Surface Shape Class categories~~

~~Once the principal curvatures are found, they can be used to calculate two other useful curvature metrics; the 'Mean' and 'Gaussian' curvatures. The Mean curvature follows directly from Euler's Theorem and is the value about which the curvature oscillates as a function of angle on the surface (Equation 3; Fig. ??).~~

~~We calculate the Mean curvature (K_M) as the average of the principal curvatures~~

$$K_M = \frac{k_1 + k_2}{2},$$

~~although it actually does not require any knowledge of the principal curvatures directly and can be calculated as the average curvature of any two orthogonal paths through a given point, an idea we will revisit in section 6 on error in Laplacian curvature. Mean curvature can also be calculated as the trace of the Shape Operator tensor~~An approach to DEM curvature analysis that utilizes the shape operator can be found in Mynatt et al. (2007) and Pearce et al. (2006), who apply a similar workflow to study

structural geologic surfaces. While this approach has greater mathematical simplicity, we find it computationally expensive to do the required matrix operations at every DEM pixel, which limits the scale over which the method can be applied. For example, on a personal laptop, the calculation of curvatures on a 1000×1000 cell DEM using a MATLAB code similar to that employed by Mynatt et al. (2007) took ~ 100 times longer than the more classical approach outlined above. Given the size of topographic datasets, decreasing computation expense increases usability of the tool.

~~The Gaussian curvature measures an intrinsic quality of surfaces that is invariant under spatial transformations that conserve distance (isometries). This means its value does not depend on the shape of the surface, but captures a more subtle quality, which is the degree of stretching or bending required to deform a flat plane so that it conforms to a given surface~~

4 Computing curvatures on gridded DEMs

4.1 Spectral filtering of gridded datasets

In order to calculate DEM curvatures, it is necessary to do some degree of smoothing. This both removes artifacts of the gridding process, (Reuter et al., 2009; Bui and Glennie, 2023; Bater and Coops, 2009) and guarantees a continuous surface (Stewart, 2003) . We use 8.1 m resolution DEM data freely available through the National Map (https://apps.nationalmap.gov/downloader/). While higher resolution LiDAR (Light Detection and Ranging) data are available in the study area, the coarser dataset is sufficient for resolving geometric trends and ridge-valley landforms at the scale of fluvial basins. ~~We compute the gaussian curvature as the product of the principal curvatures~~

$$K_G = k_1 k_2,$$

~~though more fundamentally it is the determinate of the Shape Operator tensor.~~

~~We note that while we will consistently refer to this quantity as the Gaussian curvature (K_G), in the literature it is also called the intrinsic curvature, total curvature, or sometimes just 'the curvature' in surface theory contexts (Needham, 2021) . The Mean and Gaussian curvature together can be used to classify the geometry about a point into the 8 distinct shape classes shown in Fig. 3. Since the Gaussian curvature is the product of the two principal curvatures it will only be positive in instances where k_1 and k_2 have the same sign. This tells us that when K_G is positive a surface is either a dome or basin, though because the Gaussian curvature is isometrically invariant it does not contain information about surface orientation. If K_G is negative then k_1 and k_2 necessarily have opposing signs and so the surface is locally a saddle, though again with an orientation in space that cannot be uniquely determined by the Gaussian curvature.~~ There are many established approaches to DEM smoothing, including b-spline fitting (Brigham and Crider, 2022), wavelets (Struble et al., 2024), selective denoising (Gallant, 2011), and TIN interpolation (Jordan, 2007). We choose to filter the data using a Discrete Fourier Transform (DFT; also a contribution of Gauss (Heideman et al., 1985)), which decomposes discretely sampled signals into sums of harmonic functions. Smoothing is accomplished via low-pass filtering, where information at wavelengths smaller than a defined cutoff is removed. Fourier methods have been extensively applied in geomorphology, with applications including the identification

of characteristic process scales (Perron et al., 2008), landform identification (Booth et al., 2009), and assessing topographic controls on mass transport mechanics (Richardson and Karlstrom, 2019; Black et al., 2017; Crozier et al., 2018).

~~If either k_1 or k_2~~ One challenge of Fourier methods is that harmonic functions do not naturally respect the finite nature of a DEM. Tapering of the data is thus required to obtain zero elevation at the boundaries prior to applying a DFT. It is common to accomplish this by convolving the DEM grid with a 2-d raised cosine (aka Hanning window), such that the resulting topography is equal to ~~zero then K_G is also zero. This case itself comprises its own class of surfaces, known as developable surfaces, which can be formed from a plane without altering surface area and thus are intrinsically flat. 'Relatively developable surfaces' can be extracted from the landscape by assigning a zero value to curvatures under a defined threshold (Mynatt et al., 2007). Curvature thresholding to extract developable forms is a promising approach for classifying the distribution of landforms on the Earth's surface based on curvature. However, we do not explore this further here.~~ its actual value only in center of the grid, and is elsewhere damped towards the margins (Perron et al., 2008).

~~Shape classes into which points on the surface can be sorted based on the signs on the Mean (K_M) and Gaussian (K_G) curvatures. In this analysis we focus on those classes that can be assigned based on raw curvature values, which are synformal saddles, antiformal saddles, basins, and domes, and do not include developable surfaces or perfect saddles. Modified from Mynatt et al. (2007)~~ A downside of this approach is that it does not preserve the spectral power of landscape features. Luckily, this effect can be minimized by first reflecting the topographic grid along each coordinate axis, then tapering the data only in reflected portions that fall outside the limits of the original DEM Mcnutt (1983); Harris (1978). While spurious signals at wavelengths greater than the DEM are not eliminated, this windowing approach minimizes smaller scale distortion within the study area. We use a Tukey window (implemented as *window2* in Matlab), which consists of a boxcar function convolved with a cosine taper along the margins (Harris, 1978). Tapered regions thus fall outside the extent of the original DEM.

~~The orientation of a shape in space can be determined from the Mean curvature, and so allows us to put K_G based classifications into a landscape reference frame. K_M is positive in two cases; when either both k_1~~ The Discrete Fourier Transform (DFT) is calculated as

$$Z(k_x, k_y) = \sum_{p=0}^{N_x-1} \sum_{q=0}^{N_y-1} z(p\Delta x, q\Delta y) e^{-2\pi i \left(\frac{k_x p}{N_x} + \frac{k_y q}{N_y}\right)}, \tag{24}$$

where N_x and N_y are the number of grid cells in each direction, p and ~~k_2 are positive, or the higher magnitude curvature (k_1) is positive. This means that points in the landscape with $K_M > 0$ are concave down and are locally either domes or antiformal saddles. Similarly if K_M is negative then the orientation of the surface must be dominantly concave up, and so the surface is either a basin or synformal saddle.~~ q are array indices, Δx and Δy are the grid spacings in each direction, and k_x and k_y are the wavenumbers in the respective x and y directions (Perron et al., 2008). Each value in the output array given by the above equation is associated with a frequency in x and y directions with magnitudes

$$f_x = \frac{k_x}{N_x \Delta x}, \qquad f_y = \frac{k_y}{N_y \Delta y}. \tag{25}$$

These frequencies can then be used to define a radial frequency as

$$f_r = \sqrt{(f_x^2 + f_y^2)}. \tag{26}$$

The DFT periodogram is then given by

$$P_f(k_x, k_y) = \frac{1}{N_x^2 N_y^2} |Z(k_x, k_y)|^2 \tag{27}$$

~~In cases where k_1 and k_2 are equal and opposite the surface is a perfect saddle. This too comprises its own special class of surfaces, known as 'minimal surfaces', which have been largely tied to the optimization of surface area in self-organizing systems such as soap foams, cell membranes, and crystal lattices (Osserman, 2013). The existence of approximate perfect saddles could be explored in a geomorphologic context by assigning a threshold below which curvature variation is assumed negligible. Again, we do not endeavor to explore this here.~~ Following Perron et al. (2008) we apply a half-Gaussian filter based on radial frequencies

~~Instead, we focus on the 4 basic shape classes that can be assigned based on raw curvature calculations. This will provide us with sufficient information to quantify patterns of curvature in landscapes and relate these to geomorphic process regimes.~~

$$F_{low} = \begin{cases} 1, & f < f_1, \\ \exp\left(\frac{-(f-f_1)^2}{2\sigma^2}\right), & f \geq f_1, \end{cases} \tag{28}$$

4.2 ~~Computing curvatures on gridded DEMs~~

~~An approach to surface curvature calculation for gridded DEM data that utilizes the shape operator can be found in Mynatt et al. (2007) and Pearce et al. (2006), who apply a similar approach to study structural geologic surfaces. While the mathematical simplicity of this approach is appealing, it is computationally expensive to calculate and the Shape Operator and take the trace and determinate. This in practice limits the scale over which the methods can be applied. For example, on a personal laptop the calculation of curvatures on a 1000×1000 cell DEM using a MATLAB code similar to that employed by Mynatt et al. (2007) took ~ 100 times longer than our approach. Given the size of topographic datasets, decreasing computation times makes the tool much more practical for landscape scale analysis~~where $\sigma = \frac{1}{3}|f_2 - f_1|$ is the standard deviation. The filter is convolved with the radial frequency spectrum before the filtered spectrum is reverse transformed and the original domain of the DEM is extracted from the windowed representation to yield a low-pass filtered raster of topography.

4.2 Selection of filtering scale

Once the landscape has been filtered~~all of the~~, the invariant curvature metrics outlined in ~~sections 3.1 and 3.2 are calculated for every pixel in the DEM and binned by upstream drainage area. Area is calculated at each point in the DEM~~ Sect. 3.2 and 3.1 are calculated on each DEM pixel. Curvature values are binned by drainage surface-area, calculated using the D-infinity

algorithm (Tarboton, 1997) implemented in the TopoToolbox MATLAB function library (Schwanghart and Scherler, 2014). As our approach provides a way to quantify surface area associated with each DEM via the area expansion factor α (Equation **??**) we weight DEM pixels such that we calculate the actual upstream surface area of topography rather than the area of the map-view projection. We will quantify the difference between this and the standard flow routing approach in section 6.3.

However, before exploring the landscape curvature distribution we first must choose an appropriate scale of filtering. This is accomplished by smoothing the landscape to progressively longer wavelengths, and assessing how our measures of curvature vary with scale. To eliminate any high wavenumber gridding artifacts , with pixel values weighted by the surface area ratio (α) defined in Sect. 3.1. To explore the impact of low pass filter scale, we first smooth the landscape to 50 m, then increase the low-pass filter cutoff by increments of 50 m up to 500 m . The results can be seen in Fig. 4, which shows the land surface gradient and the Gaussian and Mean curvatures binned by drainage area. While and look for shifting patterns in the area-space evolution of topographic geometry (fig. 4). While the magnitudes of curvature and slope magnitudes vary with increasing low-pass filter cutoffsvary with increased filtering, general trends in these metrics are similar across this range of filter cutoffs, making the selection of a particular scale for our analysis somewhat arbitrary. However, we note that at cutoffs greater than $\sim$ 200 m peaks in the slope curves start to get pulled to longer wavelengths suggesting a shift in the structures being resolved at those scales. We also note that. This suggests that the filter cutoff parameter does not fundamentally alter landscape geometric structure. However, while the magnitude of Mean curvatures decreases magnitudes of mean curvature decrease systematically with increasing filter cutoffthe the , the main extrema in the Gaussian curvature have highest the greatest magnitudes at a cutoff of 200 m, perhaps indicating a characteristic curvature scale in the landscape. The slope distribution also suggest this as a scale of interest, as curves are pulled to lower drainage areas up to 200 m wavelengths at which point this trend reverses.

We Based on these observations, we perform all further analysis on topography low-pass filtered to 200 m, acknowledging that this choice is somewhat non-unique. This filter scale allows us to identify landscape features that span hillslope and fluvial process regimes, however inhibits our ability to see the effects of finer scale processes (e.g., tree throw; Roering et al. (2010)). Map-view distributions of Mean mean and Gaussian curvatures, principal curvatures, tangent plane slope, and upstream drainage area for a DEM filtered to 200 m are shown in Fig. 5.

Comparison of intrinsic surface metrics use in this study with other methods common in the literature. a.Cartoon depiction of unit hemisphere used for comparison with topographic data. Red line shows curve along which error is evaluated in panel b. b.Comparison of Mean curvature (K_M) and $1/2$ Laplacian as a function of distance from the origin for plane curve defined by the intersection of the unit hemisphere with the $y-z$ plane. Black line is $1/2$ Laplacian, blue dashed line is Mean curvature calculated using intrinsic method, red dashed line is difference between $1/2$ Laplacian curvature and the curvature of the sphere ($1\ m^{-1}$), and the purple dashed line is slope of the sphere. c.% error of the $1/2$ Laplacian on the unit hemisphere and % difference between the $1/2$ Laplacian and Mean curvature on topography binned as a function of slope. Red dashed line is % error on sphere and purple boxes are median values computed on topography. d.% error of the 8 point connected gradient computed on the unit hemisphere. e.% error of the 8 point connected gradient computed on the unit hemisphere and median %

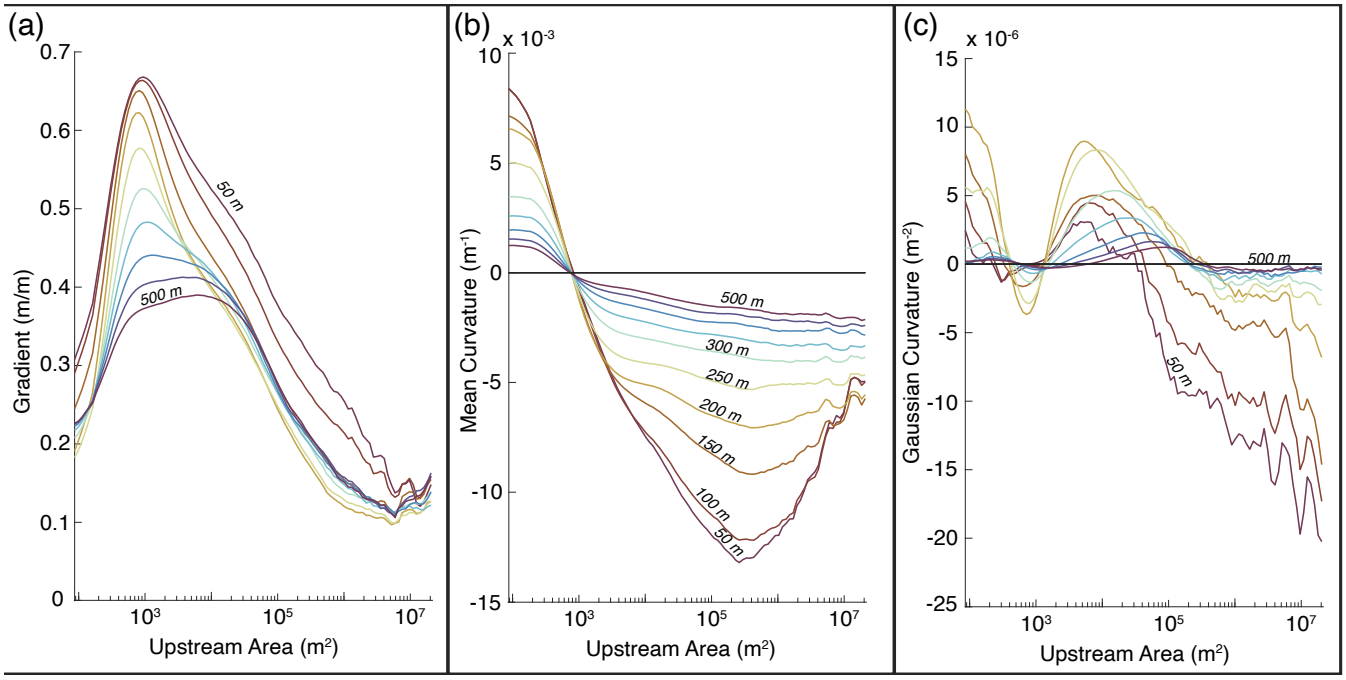

Figure 4. Surface geometry metrics binned by upstream drainage area for a range of low-pass filter cut-offs between 50 m and 500 m calculated on 50 m intervals. a. Gradient of tangent plane. **b.** Mean curvature (K_M). **c.** Gaussian curvature (K_M).

~~difference between S_8 and S_T as a function of azimuth. f.% difference between our intrinsically calculated topographic metrics and other common methods as a function of drainage area.~~

5 ~~Comparison with common methods~~ A geometric view of ~~topographic geometry calculation~~Coast Range topography

~~Applying Equations 1 and 2 to real topography requires calculation of curvature ($\nabla^2 z(x,y)$), slope ($\nabla z(x,y)$), and upstream drainage area ($A(x,y)$) from elevation data. In this work we have proposed a self-consistent approach for computing all of these metrics. We will now compare the outputs of our methods with approaches common in the geomorphology literature in an effort to identify sources of systematic error.~~

5.1 ~~Systematic error in Laplacian curvature~~

As outlined in ~~section **??** geomorphologists often take 'curvature' to be synonymous with the output of the Laplacian operator $\nabla^2 z(x,y) = z''_{xx} + z''_{yy}$, where x~~ Sect. 3.2, mean and Gaussian curvature values can be used to classify each DEM pixel uniquely into four distinct shape classes: dome, basin, synformal saddle, and ~~y are horizontal coordinates (generally easting and northing) and z is elevation. We can understand the relationship between the Laplacian and K_M through consideration of Euler's Theorem (Equation 3;l Fig. **??**), which shows that K_M is the average of curvatures measured along any two orthogonal~~

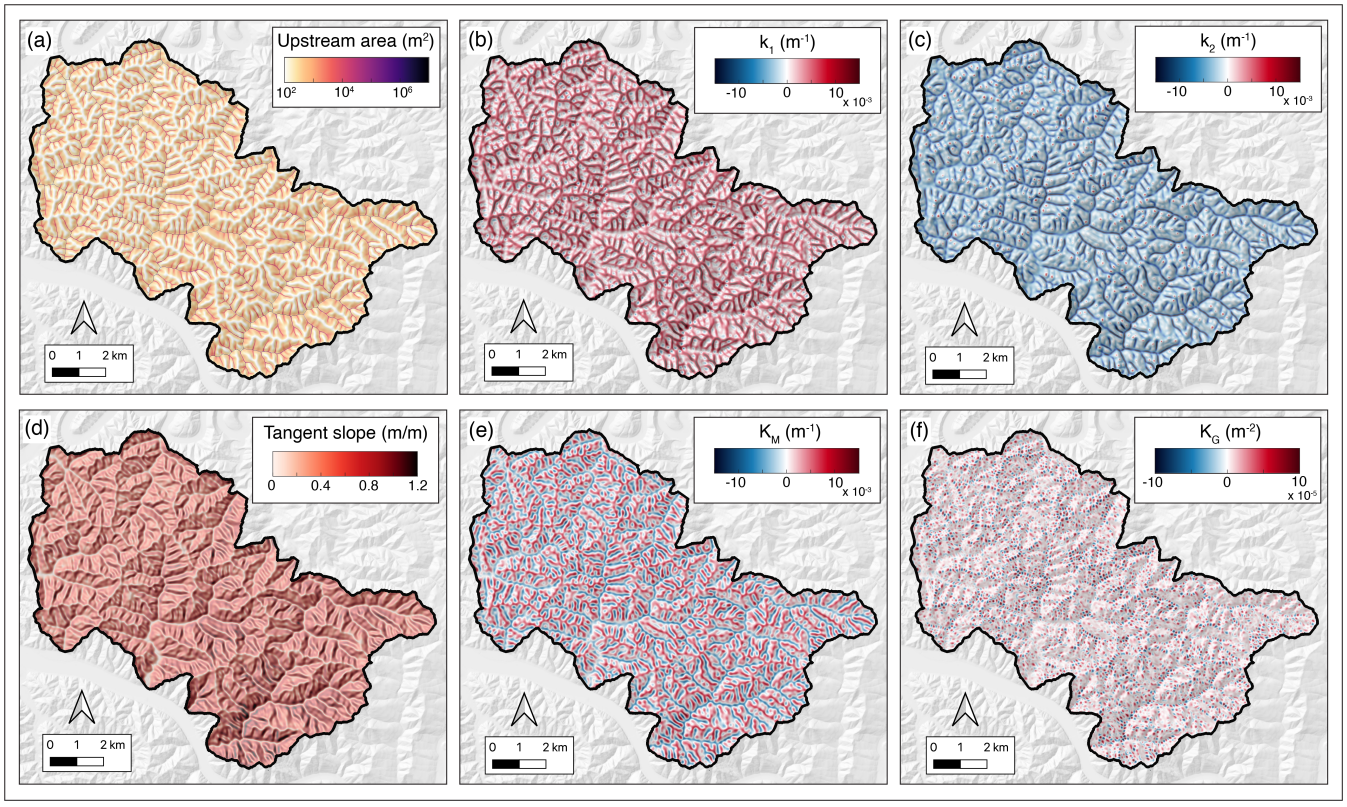

Figure 5. Map-view distributions of surface geometry metrics. a. ~~Upstream surface~~ drainage area of grid points calculated with ~~D infinity~~ D-infinity algorithm~~and weighting pixels~~. Pixels are weighted with ~~area-expansion factor~~ area-ratio α to reflect drainage area on the topographic surface rather than the map-view projection. **b.** First principal curvature (k_1). **c.** Second principal curvature (k_2). **d.** Slope of tangent plane (S_T). **e.** Mean curvature (K_M). **e.** Gaussian curvature (K_G).

paths. Thus, while our approach uses k_1 and k_2, knowledge of the principal curvatures is not required to calculate K_M. This means, if the x and y coordinate vectors are perpendicular on the surface, the relationship between the Laplacian and Mean curvatures is simply

$$K_M = \frac{z''_{xx} + z''_{yy}}{2} = \frac{1}{2}\nabla^2 z.$$

Leveraging Equation 30 allows for quantification of systematic error in the Laplacian method, which comes both from the effect of slope on derivative calculations (Bergbauer and Pollard (2003) and references therein) and the non-orthogonality of coordinate vectors on the topographic surface (section **??**; Fig. 2).

We evaluate the significance of these errors by calculating Laplacian and Mean curvatures on a unit hemisphere generated on a 1001×1001 grid in MATLAB. Since this synthetic surface has a known Mean curvature antiformal saddle ($K_M = 1/R = 1\ m^{-1}$) we can compare outputs of both the $1/2$ Laplacian and Mean curvature calculated on the grid to the analytic prediction to evaluate the accuracy of both methods. The Laplacian is calculated using the MATLAB 'del2' function, while the Mean curvature is derived using the methods of this paper. The results of this exercise can be found in Fig. 15. Fig. 15.b compares computed curvatures along the plane curve at the intersection between the sphere and the $y - z$ plane. We see that while K_M calculated using our approach (blue dashed line) maintains accuracy along the curve, the 1/2 Laplacian (solid black line) converges to the actual value only at the center of the sphere, and that error (red dashed line) increases outward with increasing slope (purple dashed curve).

To show that this sensitivity of Laplacian curvature to slope persists on topographic surfaces we define a percent error between the $1/2$ Laplacian and K_M on both the synthetic spherical surface and topography of our study area as

$$PE_{LP} = \frac{\nabla^2/2 - K_M}{K_M} \times 100.$$

On the hemisphere K_M is, at every point, the analytically predicted curvature, while on the topographic surface K_M is calculated using the methodology of this paper. Both resulting error grids are binned by tangent slope (S_T; Equation **??**) with results shown in Fig. 15. c. Median error values for the 1/2 Laplacian on topography are given by the purple boxes while error on the sphere is given by the red dashed line. We see that fractional errors in Laplacian curvature on the spherical surface are reflected in topography with errors of over 100% when slopes exceed $\sim 1\ m/m$. This shows that the Laplacian is a poor measure of curvature in steep topography, and that error magnitudes scale with the magnitude of curvature as well as slope. The dependence of Laplacian error on slope can also be seen in a plot of PE_{LP} binned by catchment area (Fig. 15.f) where a prominent spike in error up to $\sim 45\%$ occurs at drainage areas of $\sim 10^3$ m^2, which we will see in section 5.1 encompasses the steepest parts of the landscape (Fig. 7.a).

5.1 Comparison of tangent slope to 8-connected neighborhood gradient

Our approach to computing curvatures requires definition of a unit normal vector at every DEM grid cell, which can be used to define the slope of the tangent plane (S_T) via Equation **??**. While this method is mathematically equivalent to finding a

slope magnitude using the Pythagorean sum of directional derivatives it provides different information than the 8-connected neighborhood gradient method (D8) that is a default slope metric, e.g.,in the geomorphology software packages Topotoolbox (Schwanghart and Scherler, 2014) and LSDTopoTools (Mudd et al., 2019). The D8 method assigns a given pixel the slope between it and its lowest neighbor, an efficient flow routing algorithm (O'Callaghan and Mark, 1984). However its ability to accurately define the slope of a surface depends on both the orientation and complexity of the surface. To address the effects of orientation we apply the TopoToolBox D8 algorithm to the same unit hemisphere as in section 6.1 and calculate the percent error between it and the analytically defined slope (S) as

$$PE_{D8} = \frac{D8 - S}{S} \times 100.$$

Figure 15.d shows the result of Equation **??** on a map-view projection of the unit sphere. Error in computed slope varies systematically with orientation of the surface up to magnitudes of $\sim 7\%$ of the slope. In Fig. 15.e this error is binned by azimuth (black line) and compared to both the percent error between S_T and the S (blue dashed line), and the percent difference between S_T and $D8$ on topography, binned by azimuth. The percent error in S_T on the sphere is near zero, while the difference between the various slope metrics on topography tracks the azimuthal trend in D8 error on the sphere. This suggests that similar systematic error arises from D8 slope computations on DEMs. Perhaps non-intuitively, the D8 algorithm tends to underestimate slope if pixels are mis-aligned with the direction of steepest descent.

Finally, we bin the percent difference between S_T and $D8$ by catchment area to track differences in the two metrics through the fluvial network (Fig. 15.f). The highest magnitude errors ($\sim 35\%$) occur on ridges (section 5.1.1), while the next highest magnitude negative errors ($|> 20\%|$) occur at the highest drainage areas within the fluvial network (section 5.1.4). We will see in section 5.1 that this trend tracks that of Mean curvature (Fig. 7.b) suggesting sensitivity of the D8 algorithm to surface curvature as well as orientation.

5.1 Catchment surface area versus map-view area

As outlined in sections **??** and **??** the intrinsic formulation of surface geometry is partially motivated by the fact that distances on a sloped surface are greater than distances on their 2-d map representation. This means that pixel dimensions used to compute catchment area in flow routing algorithms underestimate area on the topographic surface by the area expansion factor α defined by Equation **??**. To evaluate the effect of projection distortion on catchment area calculations we compute two separate area grids. Using the D-Infinity flow routing algorithm in TopoToolbox (Schwanghart and Scherler, 2014) we calculate a standard extrinsically derived upstream area (A_E) using DEM pixel dimensions to assign an area to each grid cell. We also compute the intrinsically derived upstream area (A), in which we use the same algorithm but pixel areas are weighted by α to give the true area of the surface within each pixel. We once again define a percent difference as

$$PE_A = \frac{A_E - A}{A} * 100$$

and plot the result binned by drainage area in Figure 15.f. Through most of the landscapeextrinsic catchment area calculations underestimate catchment surface area by $10 - 15\%$, with potential implications for the interpretation of continuity equations.

6 ~~Geometric view of Coast Range topography~~

~~As outlined in section 3.2, the Mean and Gaussian curvatures can together classify each DEM pixel uniquely into one of four distinct shape classes. We compute these classifications for our study site, and in this section discuss the resulting distributions in terms of curvature metrics as function of contributing drainage area. We will argue that this approach effectively maps curvature onto known fluvial erosion process regimes (Montgomery and Foufoula-Georgiou, 1993).~~

3). We find that upstream drainage area provides a natural way to study the resulting shape class distributions across the landscape, represented in Fig. 6.~~b shows a~~ a by its probability density function (PDF)~~for each of the four shape classes as a function of contributing drainage area, which is~~ . Figure 6.b shows PDFs of each shape class, which represents the probability of a shape class and given drainage area value occurring simultaneously ($P(C \cap A)$). ~~Comparison to the drainage area PDF (Fig. 6.a) shows that shape probabilities strongly vary with the likelihood of a given drainage area . For comparative purposes it is~~ As the distribution of shapes is clearly weighted by the area distribution, we find it more informative to calculate the conditional ~~probability, which we do~~ probabilities of shapes classes (Fig. 6.c) by invoking the probability axiom ~~(Dekking et al., 2005)~~

$$P(C \cap A) = P(C|A)P(A) \rightarrow P(C|A) = \frac{P(C \cap A)}{P(A)}, \tag{29}$$

where ~~$P(A)$ is the probability of pixel having a given upstream area.~~ $P(C|A)$ is the conditional probability ~~(Fig. 6.c), or probability of a given~~ of shape class occurring ~~at a point with a given upstream area (?). This can be used to demonstrate how land surface geometry records process transitions in fluvial landscapes.~~ given a value of A, and $P(A)$ is the probability of pixel having a drainage area A.

Figure 7 shows a compilation of basic geometric data extracted through our approach, represented in both area-space and map-view perspectives. While other potentially useful information can be extracted using this approach (such as the orientations and magnitudes of k_1 and k_2), we focus largely on curvature invariants to demonstrate the utility of curvature for identifying distinctive geometric properties of fluvial topography.

~~Fig. 7 shows the the distributions of slope, area, Mean and Gaussian curvatures, and surface shape classes in area-space, as-well-as the distribution of shape classes in map view. In Fig. 7.d we see that the landscape is evenly partitioned into concave up and concave down geometric structures implying a landscape organizational signal reflected in Mean curvature that will be discussed further in section 5.2.~~

5.1 Landscape partitioning from Gaussian curvature

Noting significant and systematic variation in shape class distributions and curvature metrics with upstream drainage area (Fig. 7.a-c), we ~~demonstrate a landscape segmentation approach~~ now explore landscape segmentation using inflection points ~~(zero crossings) of the two curvature invariants. This approach~~ in the mean and Gaussian curvatures. This is motivated by ~~physical theory, as the~~ the physical assumption that signs of both K_M and K_G have implications for mass transport phenom-

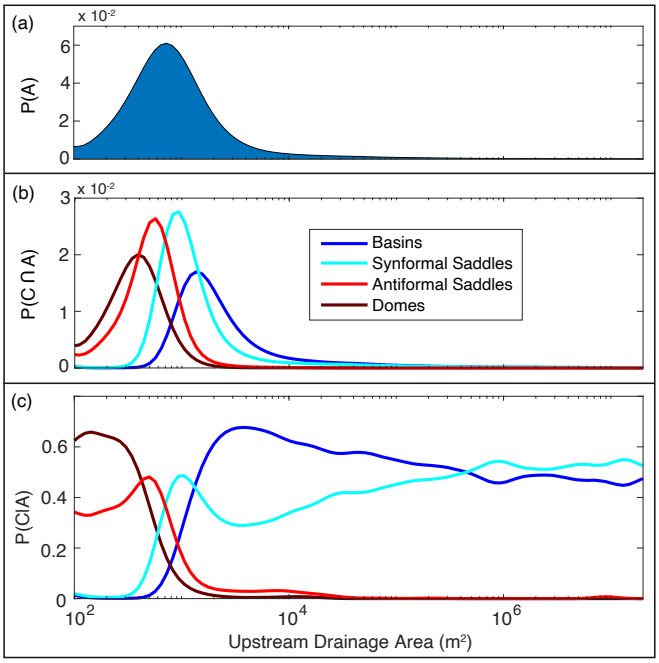

~~Shape class distributions as a function of drainage area. a. Probability density function of upstream drainage areas within the study area. b. Probability density functions of shape classes as a function of drainage area. c. Conditional PDFs of shape classes at a given drainage area.~~

Figure 6. Shape class distributions as a function of drainage area. **a**. Probability density function of drainage areas within the region of interest. **b**. Probability density functions of shape classes as a function of drainage area. **c**. Conditional PDFs of shape classes at a given drainage area.

ena. The sign of K_M records the divergence versus convergence of local gradients, while the sign of K_G differentiates between stable and unstable 'critical points' ~~with theoretical implications for~~ that influence how the surface ~~respond to disturbances (Goldsten et al., 2002; Matsumoto, 2001)~~responds to disturbances (Goldsten et al., 2002; Matsumoto, 2001; Bonetti et al., 2018) . As our partitioning approach is ~~geometrically motivated~~ rooted in geometry we choose a labeling scheme Σ_i^j based solely on ~~geometry~~curvature invariants. Subscripts indicate the curvature ~~invariant~~ used ($i = G$ for K_G and $i = M$ for K_M), while superscripts (j) correspond to the number of previous zero crossings in area space ($j = 0$ corresponds to the zero crossing at smallest drainage area). This ~~provides a convenient~~ reference for curvature domains ~~expressed as portions of a landscape, and could~~ should facilitate future comparative studies ~~that explore differences in the relationship between geometry and process~~ of geometry across diverse tectonic, climatic, and lithologic settings.

5.1.1 Σ_G^0: ~~Drainage~~ drainage areas less than ~~3.75×10^2~~ 3.50×10^2 m^2

In fluvial landscapes, the smallest drainage areas are associated with the ridge-peak networks ~~that separate~~ separating neighboring watersheds (Scherler and Schwanghart, 2019). We define a landscape region (~~that we call~~ Σ_G^0) containing ~~all land~~

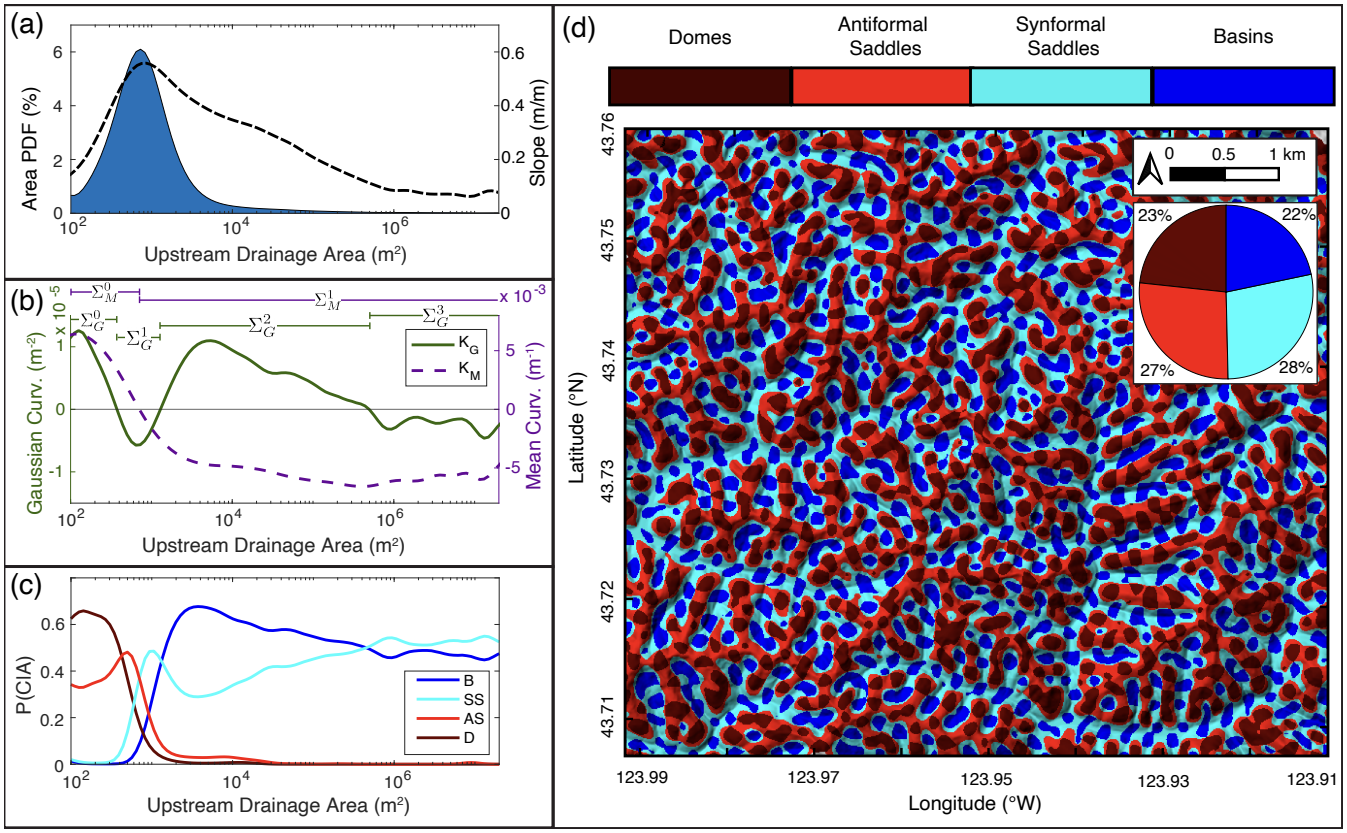

Figure 7. Distribution of derived surface geometry metrics computed on the full region of interest. **a)** PDF of upstream drainage areas. Black dashed curve is slope binned by drainage area. **b)** Gaussian and mean curvatures binned by ~~upstream~~ drainage area. Horizontal lines at top of panel show Σ regions outlined in ~~sections~~ Sect.s 5.1 and 5.2. **c)** Conditional PDFs of shape classes as a function of ~~upstream~~ drainage area. **d)** Map of shape classes projected on a focused subregion of the study area. ~~Pie chart~~ Pie-chart inset shows shape-class composition of the surface.

~~surface points~~ pixels with drainage areas less than 3.75×10^2 m^2, ~~a value coincident with~~ the first area-space inflection in Gaussian curvature (Fig. 8.b). In this region~~both the Mean and Gaussian curvatures~~ , both curvature invariants are dominantly positive, reflecting downward concavity of topography and the divergence of surface gradient vectors ~~(O'Neill, 2006)~~ (Dietrich et al., 1993; O'Neill, 2006). This is consistent with ~~the idea that ridge networks lack~~ a region lacking convergent overland flow (Fenneman, 1908), ~~and so~~ where mass transport is accomplished through diffusive ~~processes with rates that scale with curvature and site-specific diffusivity (Roering et al., 1999a). Thus high magnitude positive Mean curvatures in this region indicate~~ hillslope-transport processes. Large positive mean curvature here suggests high rates of ~~diffusive mass transport, likely~~ diffusion required for erosion along ridge lines to keep pace with ~~advective~~ mass transport in channel networks below ~~. This idea~~ (Roering et al., 1999b). This is supported by ~~well documented~~ correlations between Laplacian ~~hilltop curvature and catchment-scale erosion rates~~ curvature of hilltop regions and drainage-scale erosion rates elsewhere in the Oregon Coast

Range , where curvature is usually calculated as the Laplacian operator applied to isolated hilltop regions (Struble et al., 2024) . Our approach allows for physics-informed delineation of this diffusion-dominated region, while robustness of our approach against systematic slope and curvature dependent error (section 6) allows for continuity in topographic geometry calculations between this high curvature region and the steeper hillslope domain below (Roering et al., 2001a). (Struble et al., 2024).

The map-view representation of the Σ_G^0 region (Fig. 8.d) shows the spatial distribution of diffusion dominated regions with implications for the organizational structure of fluvial landscapes. According to this partitioning schemeDefined this way, the ridge-peak network makes up 19% of the land surface area, with 63% of surface points making up localized dome structures 18% of the land-surface (to 2 significant figures). Within this subregion, 63% of points are domal (peaks)that are connected by , with antiformal saddles (ridges) that comprise the remaining 37% comprising the remaining 37% (Fig. 8.a,d). Transitions between these shape classes along ridge lines show Along ridge lines this is expressed in oscillations between positive and negative Gaussian curvatures, analogous to the alternating "summits" and "knots" of Cayley (1859)Cayley (1859), and the "hills" and "passes" of Maxwell (1870)Maxwell (1870). We will elaborate on this connection to early landscape organization theories in section Sect. 5.3.

5.1.2 Σ_G^1: Drainage areas between ~~3.75×10^2~~ 3.50×10^2 m^2 and 1.29×10^3 m^2

As drainage area increases beyond 375 above 350 m^2, the binned Gaussian curvature changes sign and remains is negative up to drainage areas of 1290 m^2 (Fig. 9.b). This region (Σ_G^1) makes up the majority of the landscape with 54% of pixels falling in Fifty-seven percent of the land surface falls within this relatively narrow range of catchment areas. This is also the steepest landscape region drainage areas, making it the largest of the Σ_G^j. This region is defined by high topographic gradients (Fig. 9.a), coinciding with hillslopes where loose material moves downhill through a combination of gradient driven processes such as gradient-driven landsliding, granular creep, and stochastic particle dislocation (Roering et al., 2001b; Jaeger and Nagel, 1992; Furbish et al .

Here the landscape undergoes a major concavity transition between raveling (Roering et al., 2001b; Jaeger and Nagel, 1992; Furbish et al., . Within this region, the point of minimum K_G coincides with the highest slopes in the landscape. It is associated with the only inflection point in mean curvature, marking the dominant concavity transition in the landscape. Such a concavity transition is required to connect almost uniformly divergent topography on hilltops (Σ_G^0; section 5.1.2) and Sect. 5.1.1) to convergent basins at the head of the convergent drainage network (Dietrich et al., 1993). This region contains the Mean curvature's only area-space inflection point at 740 m^2, which is aligned with the global minimum in binned Gaussian curvature and global maximum in topographic slope (Fig. 9.a-bdrainage network (Σ_G^2; Sect. 5.1.3). Geometrically, this transition is seen in the rapidly evolving manifests as rapid shape-class distributions in changes over a small range of drainage area (Fig. 9.cwhich suggest) and a more even split between the four shape classes overall (each shape class occupies $\sim 10-30\%$ of the region), which suggests a high level of surface complexity across this concavity transition; complexity that is not captured by analyses of hillslopes conducted along 1-d profiles (Roering et al., 2001a), but perhaps is better captured by approaches that leverage ,

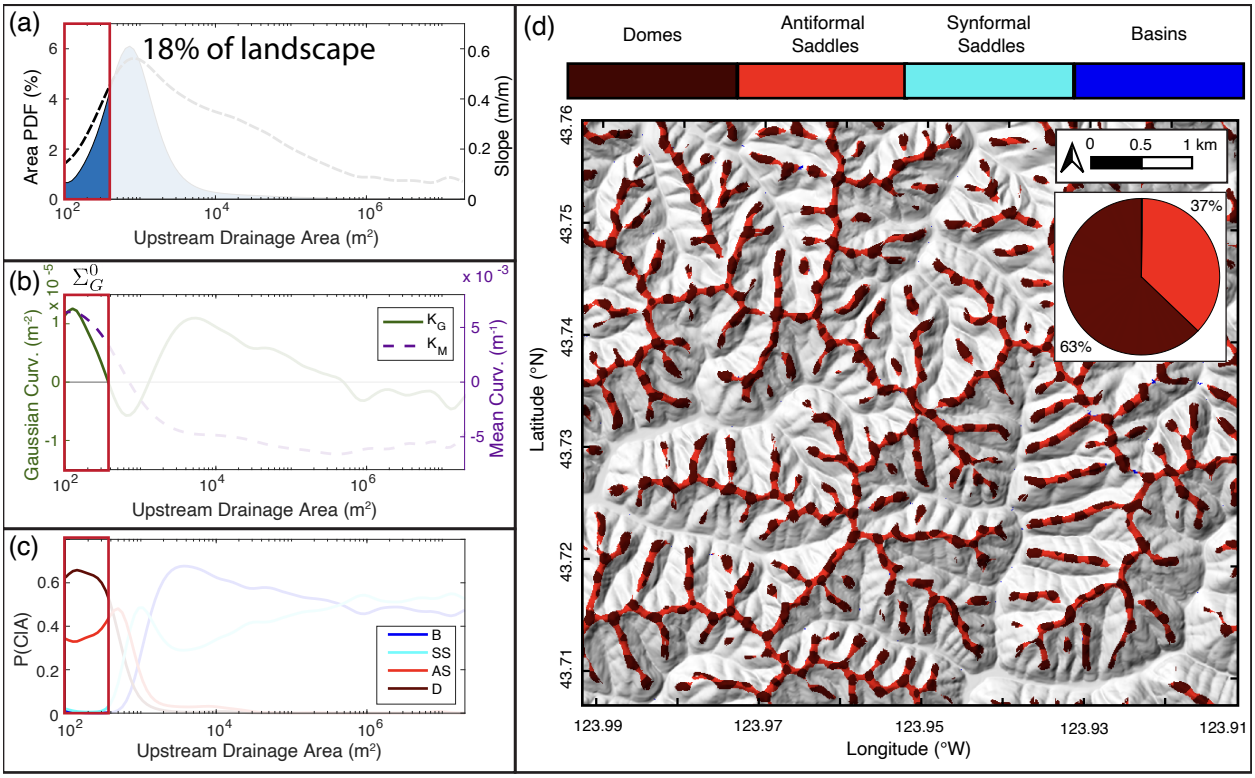

Figure 8. Surface geometry data for region Σ_G^0: points in the landscape with upstream drainage areas less than ~~3.75×10^2~~ 3.50×10^2 m^2. The red box in each of the area-binned plots (a-c) highlights the range of included drainage areas. **a)** PDF of ~~upstream~~ drainage areas. **b)** Gaussian and ~~Mean~~ mean curvatures binned by ~~upstream drainage~~ area. **c)** Conditional PDFs of shape classes~~as a function of upstream drainage area~~. **d)** Map of shape classes projected on a focused subregion of the study area. ~~Pie chart~~ Pie-chart inset shows shape-class composition of the surface.

consistent with previous inference based on topographic contour curvature (Bonetti et al., 2018). ~~In section 5.2 we will show a landscape partitioning scheme based on this concavity inflection, which may itself represent a strong landscape organization signal.~~

5.1.3 Σ_G^2: ~~Drainage~~ drainage areas between 1.29×10^3 m^2 and ~~3.30×10^5~~ 3.80×10^5 m^2

At drainage areas of 1.29×10^3 m^2~~the binned~~, the Gaussian curvature again changes sign, increasing to a local maximum at ~ 4500 m^2 before steadily ~~decreasing back~~ returning to zero at 3.30×10^5 m^2 (Fig. 10.b). We define our third landscape region (Σ_G^3) between these inflection points. Here, convergence of surface gradient vectors is indicated by negative K_M and the dominance of basins (60%) and synformal saddles (36%). ~~In map view (Fig. 10.d) the existence of basins at the smallest drainage areas are likely the geometric expression of colluvial hollows~~This geometry intuitively implies colluvial hollows, where unconsolidated material collects at the head of debris-flow networks (Dietrich et al., 1993). ~~As drainage area increases~~

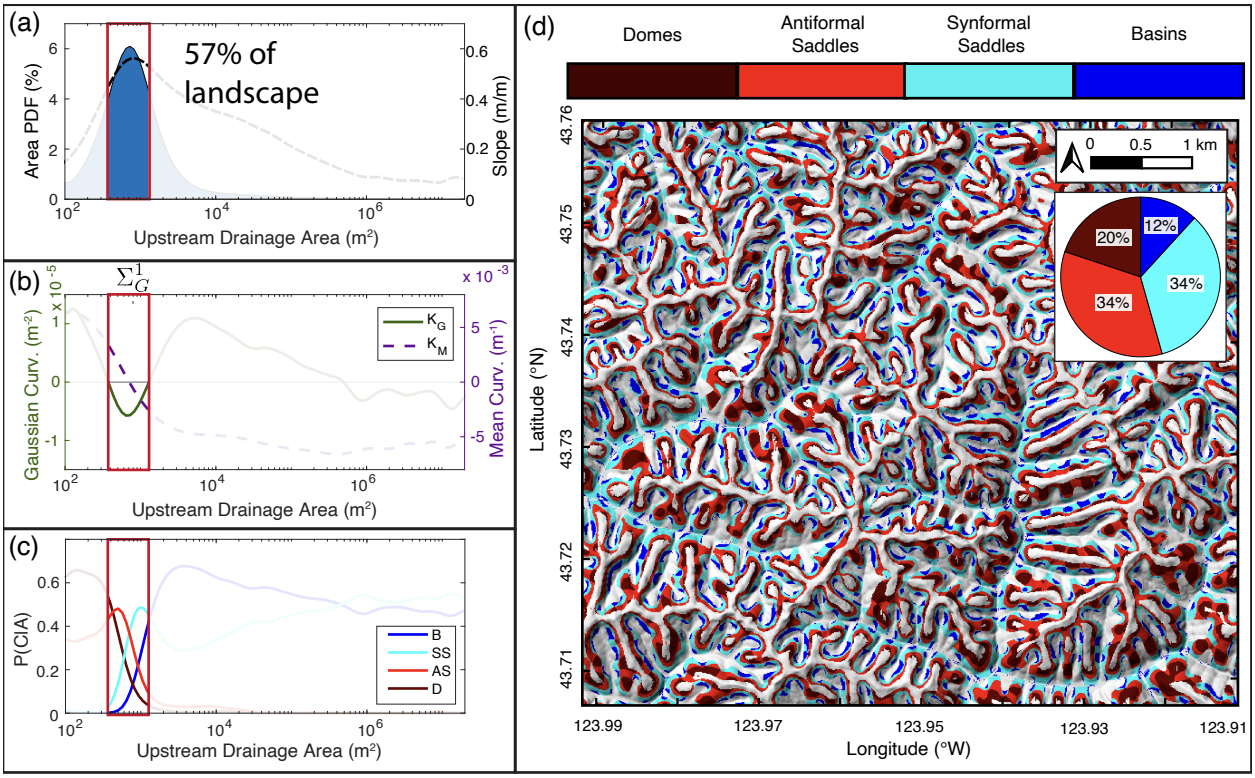

Figure 9. Surface geometry data for region Σ_G^1: points in the landscape with upstream drainage areas between ~~3.75×10^2~~ 3.50×10^2 $\mathbf{m^2}$ and 1.29×10^3 $\mathbf{m^2}$. The red box in each of the area-binned plots (a-c) highlights the range of included drainage areas. **a)** PDF of ~~upstream~~ drainage areas. **b)** Gaussian and ~~Mean~~ mean curvatures binned by ~~upstream drainage~~ area. **c)** Conditional PDFs of shape classes~~as a function of upstream drainage area~~. **d)** Map of shape classes projected on a focused subregion of the study area. ~~Pie chart~~ Pie-chart inset shows shape-class composition of the surface.

~~past the~~ At drainage areas exceeding that of the local maximum in Gaussian curvature~~the consistent negative slope in both the Gaussian and Mean curvatures~~ , the decrease in both K_G and K_M is consistent with increasing downstream channelization in debris-flow channels (Stock and Dietrich, 2003; Mcguire et al., 2022). This same trend is apparent in the shape class distributions in Fig. 10.c~~where a decrease in basin points trades off with an increase in synformal saddles as the landscape becomes increasingly convergent.~~

, where basins trade off with synformal saddles surface gradient vectors converge. This region makes up ~~20%~~ 25% of the study area, ~~similar to the 19%~~ slightly more than the 18% of the landscape encapsulated by the other region of positive Gaussian curvature (Σ_G^0, the ridgeline network). In addition, the percent composition of basins (~~60%~~60%) and synformal saddles (~~36%~~36%) roughly mirrors the Σ_G^0 composition of domes (~~63%~~63%) and antiformal saddles (~~37%~~) . ~~This symmetry in curvatures~~ 37%) in Σ_G^0, a symmetry that will be discussed further in ~~section~~ Sect. 5.2.

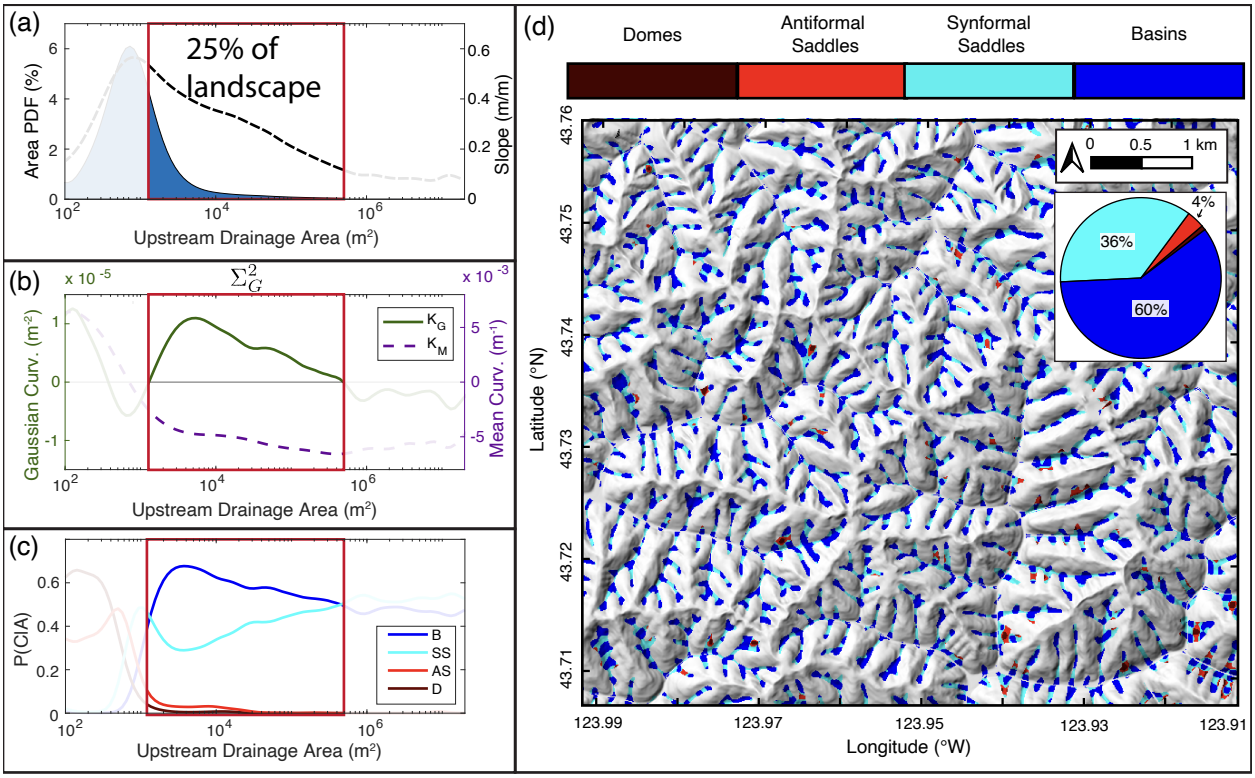

Figure 10. Surface geometry data for region Σ^2_G: points in the landscape with upstream drainage areas between 1.29×10^3 m^2 and ~~3.30×10^5~~ 3.80×10^5 m^2. The red box in each of the area plots highlights the region of interest. **a)** PDF of ~~upstream~~ drainage areas. **b)** Gaussian and mean curvatures binned by ~~upstream drainage~~ area. **c)** Conditional PDFs of shape classes~~as a function of upstream drainage area~~. **d)** Map of shape classes projected on a focused subregion of the study area. ~~Pie chart~~ Pie-chart inset shows shape-class composition of the surface.

5.1.4 Σ^3_G: ~~Drainage~~ drainage areas greater than ~~3.30×10^5~~ 3.80×10^5 m^2

The last inflection point in ~~binned~~ Gaussian curvature occurs at drainage areas of ~~3.30×10^5~~ 3.80×10^5 m^2, where synformal saddles surpass basins as the dominant morphology (Fig. 11.c). ~~This intuitively implies a~~ The growing influence of channels in defining landscape ~~curvatures, and so we associate this final region (Σ^3_G) with the fluvial network, noting that drainage areas between 10^5 and 10^6 m^2 are commonly associated with the onset of fluvial processes (Montgomery and Foufoula-Georgiou, 1993) . In terms of surface area the~~ curvature suggests the dominance of fluvial erosion, an interpretation that is consistent with area-space fluvial transitions inferred elsewhere in the literature (Montgomery and Foufoula-Georgiou, 1993). The spatial contribution of this region is ~~small (7%~~extremely small ($< 1\%$ of the land surface; Fig. 11.a), with little geometric change across the two orders of magnitude spanned by drainage area. The only overall trend is a gradual increase in ~~Mean~~ mean curvature, which ~~is consistent with~~ could indicate downstream valley widening as erosional efficiency ~~of river channels increase with drainage area~~increases. However, a ~~detailed~~ close look at the map-view shape distribution (Fig. 11.d) reveals regular transitions

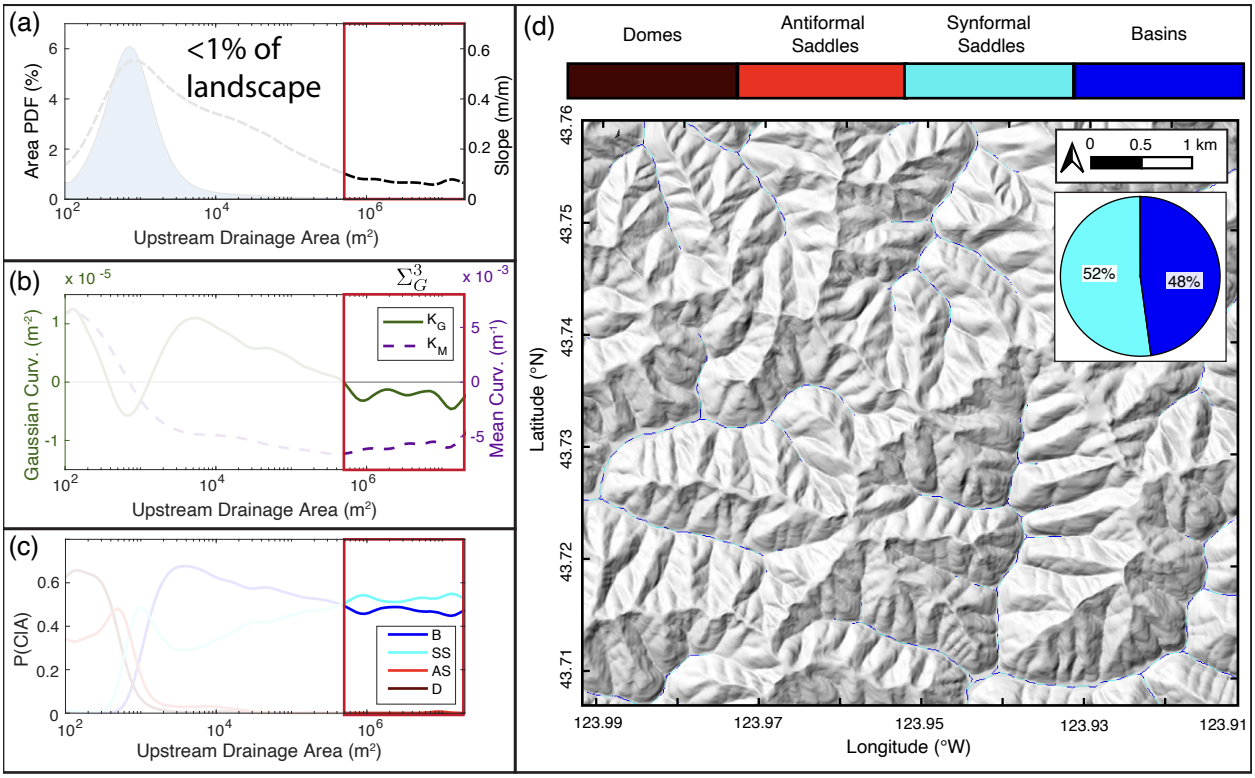

Figure 11. Surface geometry data for region Σ^3_G: points in the landscape with upstream drainage areas ~~between 4.5×10^3~~ greater than 3.80×10^3 m^2 ~~and 9.8×10^5 m^2~~. The red box in each of the area plots highlights the region of interest. **a)** PDF of ~~upstream~~ drainage areas. **b)** Gaussian and ~~Mean~~ mean curvatures binned by ~~upstream drainage~~ area. **c)** Conditional PDFs of shape classes~~as a function of upstream drainage area~~. **d)** Map of shape classes projected on a focused subregion of the study area. ~~Pie chart~~ Pie-chart inset shows shape-class composition of the surface.

between basin and saddle structures, indicating along-channel oscillations in the first principal curvature (k_2 is always negative in a channel) – another observation connecting our analysis to the ideas of Cayley and Maxwell that we will revisit and discuss in ~~section~~ Sect. 5.3.

~~All~~ While all of the process regimes identified in this Gaussian curvature decomposition have been previously identified in the literature ~~(Montgomery and Buffington, 1997). However~~ (e.g.Montgomery and Buffington (1997)), it is remarkable ~~that a single topographic metric can capture~~ how clearly this single intrinsic metric captures the full range of process transitions in a fluvial landscape. ~~Tracking the Gaussian and Mean curvatures simultaneously through area-space suggests ways to constrain geomorphic processes in transitional portions of landscape that are difficult to characterize with extrinsically derived geometry metrics.~~

5.2 Landscape partitioning from ~~Mean~~ mean curvature

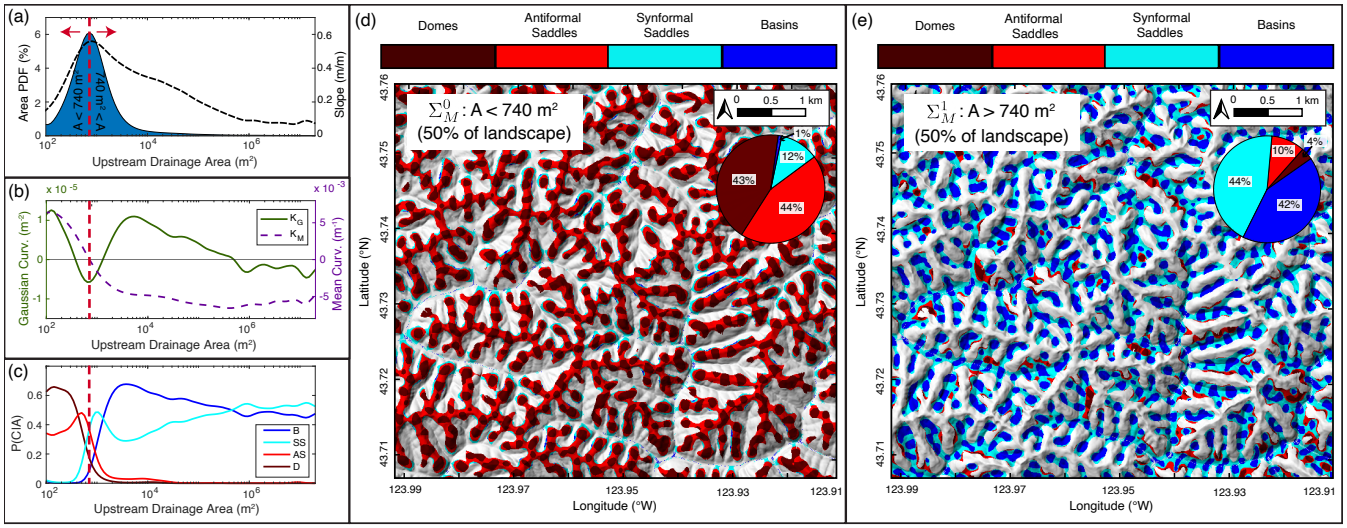

Figure 12. Maps of surface geometry for landscape partitioning about the ~~Mean~~ mean curvature inflection point at drainage areas of ~~740~~ 740 m~~^{2}~~^{2}. Red-dashed lined shows location of curvature inflection point. a.~~)~~ PDF of ~~upstream~~ drainage ~~area~~areas. ~~Dashed red line shows point of landscape partitioning.~~ **b)** Gaussian and mean curvatures binned by ~~upstream drainage~~ area. **c)** Conditional PDFs of shape classes~~as a function of upstream drainage area~~. **d)** Map of shape classes for ~~areas of the landscape with~~ drainage areas ~~greater~~ less than 740 m~~^{2}~~^{s}. ~~Pie chart inset shows shape-class composition of the surface.~~ **e)** Map of shape classes for ~~areas of the landscape with~~ drainage areas ~~smaller~~ greater than 740 m~~^{2}~~^{s}. ~~Pie chart inset shows distribution~~ Pie-chart insets on panels d and e show shape-class compositions of ~~shape classes~~the surfaces.

~~Section 5.1 demonstrates that Gaussian curvature inflection points effectively classify landscape process transitions.~~ In this section we show that ~~Mean~~ mean curvature also provides a ~~useful segmentation scheme~~way of understanding connections between geometry and process in fluvial topography. We decompose the landscape into two regions (Σ_M^0 and Σ_M^1) separated by the single inflection in K_M at drainage areas of ~~740~~ 740 m^2. Results are shown in Fig. 12. Alignment between this ~~curvature inflection point~~ point in area-space and the peak of the slope curve in Fig. 12.a is consistent with the idea that curvature decreases as hillslope profiles approach an angle-of-repose ~~above which slope are gravitationally unstable Roering et al. (2007)~~ ($\sim 30°$; peak of the slope curve in Figs. 7-11), above which loose material is gravitationally unstable (Roering et al., 2007). Downhill of this point, slope decreases and unconsolidated material will tend to collect as colluvium at the head of the channel network (region Σ_G^2).

~~The landscape is equally distributed about this zero crossing such that 50% of points are above/below the most probable drainage area value in our study area.~~ Partitioning the landscape this way reveals surprising symmetries in both shape class distributions and surface geometry metrics ~~of~~ for the two regions (Fig. 12.d-e). The landscape is equally distributed about this zero crossing. For our filtering method and scale, 50% of points are above or below the most probable drainage area value in our study area. Figure 13.a shows a map of the study area divided into concave and convex domains based on this area threshold.

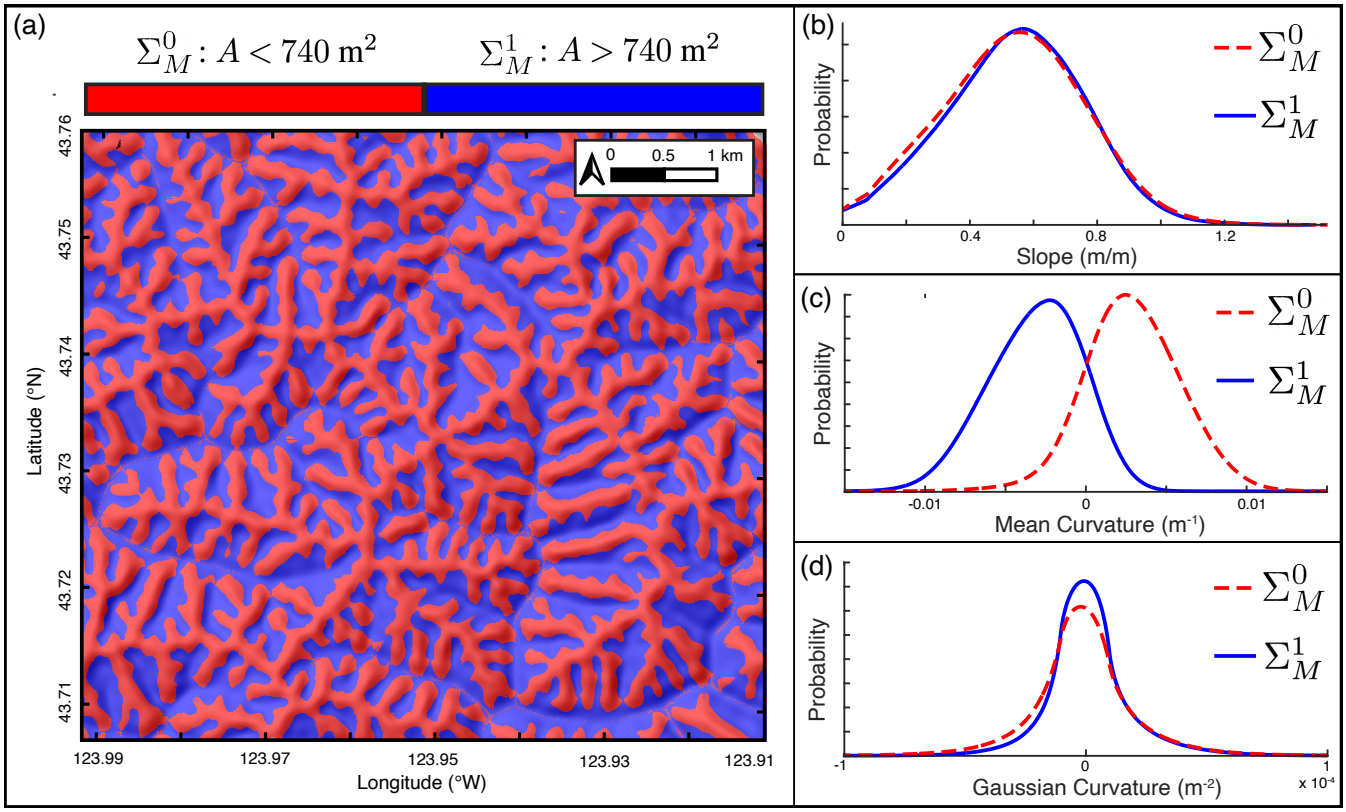

Figure 13. Distribution of surface geometry metrics for regions defined by the ~~Mean~~ mean curvature inflection point. a. Map-view of landscape partitioned about the point of inflection in K_M. **b.** Distribution of tangent slope in regions of both negative and positive average K_M. **c.** Distribution of ~~Mean~~ mean curvature in regions of both negative and positive average K_M. **d.** Distribution of Gaussian curvatures in regions of both negative and positive average K_M

Probability distributions of slope, ~~Mean~~ mean curvature, and Gaussian curvature for the two regions are shown in Fig. 13.b-d. While the slope and Gaussian curvature are similarly distributed in the concave and convex landscape regions, we see that the ~~Mean curvature is distributed symmetrically~~ mean curvature has mirrored distributions such that the ~~total Mean~~ integrated mean curvature in the landscape is ~~close to zero. This observation could be interpreted as reflecting a "Minimal Surface" condition (Han and Che, 2018) for steady state landscapes, in which total Mean curvature is minimized. Making quantitative process-based connections to Minimal Surface theory is beyond the scope of this paper, however.~~ approximately zero.

5.3 Geometric properties of channels and ridges

We have thus far focused on documenting Oregon Coast Range landscape segmentation in drainage area from a curvature perspective. A clear corollary to this is to ask specifically about the emergent channel and ridge network structures that manifest from this drainage area segmentation. It is well established that curvature provides a powerful tool for extracting continuous

concave-up structures and deriving definitions of channel networks that are self-consistent throughout the landscape (Passalacqua et al., 2010; Gallant and Hutchinson, 2011; Bonetti et al., 2018). Our methods are suitable for this task as well, and for the parallel extraction of concave-down ridge network structures (Scherler and Schwanghart, 2019), but we will not pursue that objective here.

Instead, we will focus on the strikingly even partitioning of ~~Mean~~ mean curvature between concave up structures (channels) and concave down structures (ridges). These structures are themselves composed entirely of alternating basins and synformal saddles (in channels) and domes and antiformal saddles (on ridges). Figure 14.a shows a close-up of our study area around Franklin Creek to demonstrate this pattern. While the size distribution of these alternating shape classes within a channel or ridge is variably sensitive to lowpass filter threshold, the shape classes themselves are much more robust as they reflect zero crossings in K_M and K_G whose positions are insensitive to filter cutoff (Fig. 4), particularly in the case of mean curvature. This alternating pattern of local shape classes, originally recognized qualitatively by Cayley (1859) and Maxwell (1870)~~seems to be a fundamental aspect of~~ , manifests clearly in channel and ridge network geometry.

Fig. 14.b-c plots in blue the elevation of Franklin Creek and its south ridge as a function of distance from the most downstream point of the creek (where it intersects the Umpqua river). The drainage area (red curves) along these structures (calculated using the intrinsic area calculation method in ~~section~~ Sect. 6.3) reflects expectations: discontinuities in drainage area along the channel correspond to tributary junctions while ridge-top drainage area deviates from one grid cell only in saddles (up to 8 grid cells long here) between local maxima.

Fig. 14.d-e plots the signed principle curvatures for ridge and channel. An immediate comparison of note is that local minima in k_1 for the channel and k_2 for the ridge correspond to basins and antiformal saddles respectively (circles). These structures align with tributary junctions in the channel, and lie directly upslope of 1st order channel heads on the ridge. This indicates that the curvature shape classes reflect structural changes in network geometry for both concave and convex topography. Neither structure – the local basins at channel junctions or saddles on ridgetops corresponding to transitions from hillslopes to channels – have been previously described to our knowledge. As these geometries describe changes in curvatures associated with branching structures in channels and ridges their locations are minimally sensitive to filter cutoff.

Fig. 14.f-g then plots the Gaussian (K_G) and ~~Mean~~ mean (K_M) curvatures along the channel and ridge. The notable comparison in this case is that local maxima in K_G and K_M are anticorrelated along the channel and correlated along the ridge. This symmetry reflects the paired shape classes in either structure.

~~In comparing~~ Comparing channel and ridge geometries we see that, in both cases, the two measures of curvature (principle curvatures or invariants) are near mirror-images of each other. ~~In both cases one~~ One metric oscillates around zero (a principle curvature in 14.d-e and K_G in 14.f-g), while the other is strictly positive (for ridge) or negative (for channel), although still oscillatory. The along-channel and along-ridge envelope of this latter metric varies non-monotonically ~~, as to be~~ as expected for a small dendritic drainage basin, but ~~nonetheless~~ also exhibits coincident channel widening (decrease in the magnitude of k_2) and ridge narrowing (increase in k_1 towards the mouth of Franklin Creek (distances $\lesssim 2300$ m).

Finally, while ~~physics-based~~ process-based modeling of curvature is outside the scope of this work, it is informative to compare the observed curvature of channel and ridge to theoretical models. Fig. 14.c-E show best fitting ~~powerlaws~~ power laws to ridge and channel, after (Whipple and Tucker, 1999) for bedrock channel longitudinal profile and models such as those of Willett (2010) for interfluvial ridge elevations. The fit constants are $a = 6$ m, $b_1 = 2.84 \times 10^{-7}$ m$^{-1.4}$, $c_1 = -1.4$, $b_2 = 41.88$ m$^{0.72}$, $c_2 = 0.28$.

For Franklin Creek, while the elevation profile is ~~well-fit~~ well-approximated by a stream power-law fit, the resulting curvature (obtained by differentiating the longitudinal profile twice with respect to alongstream distance x) does not capture oscillations observed in k_1, the along-channel principal curvature. And yet the average value of the stream power model curvature (1.1×10^{-5} m^{-1}) is close to the average value of k_1 (8.3×10^{-5} m^{-1}) extracted from the DEM (we expect an even closer match if tributaries are included in the stream power model, e.g., Willett (2010)). Thus, the steady state model approximates the average concavity of the true channel geometry, despite much larger curvature oscillations associated with local basin structures at tributary junctions.

Similarly, a power-law fit to the Franklin Creek south ridge profile in Fig. 14.c well represents the elevation but ~~misses~~ fails to capture the smaller scale curvature oscillations oscillations between domes and antiformal saddles. The average value of this fit (-3.3×10^{-4} m^{-1}) is ~~with~~ within 7% of the average value of k_2 (-3.5×10^{-4} m^{-1}) extracted from the DEM, reflecting the overall concave down nature of the along-ridge curvature. These results suggest that standard fluvial process models, while missing physical ingredients at smaller scale, capture network-scale curvatures of channels and ridges.

6 Comparison to common metrics of topographic geometry

In this work, we have proposed a self-consistent means of defining several geometrical aspects of topography through connection to formal surface theory. We will now draw quantitative comparisons to some other commonly used metrics. We do this in an effort to highlight potential advantages of the invariant approach acknowledging, of course, that simpler methods are sometimes appropriate. Our goal is not to supplant other approaches, but rather to point out opportunities for increased adoption of an intrinsic reference frame in topographic analysis.

6.1 Comparison of mean and Laplacian curvatures

As outlined in Sect. 1.1, 'curvature' in geomorphology is often taken as synonymous with the output of the Laplacian operator, which arises from mass-continuity equations on hillslopes (Fernandes and Dietrich, 1997). We can understand the relationship between the Laplacian and K_M through consideration of Euler's Theorem (Eq. 3), which shows that K_M is the average of curvatures measured along any two orthogonal paths on the surface. In cases where the x and y coordinate vectors are perpendicular on the surface, the relationship between the Laplacian and mean curvatures is (compare to equation 4 which uses

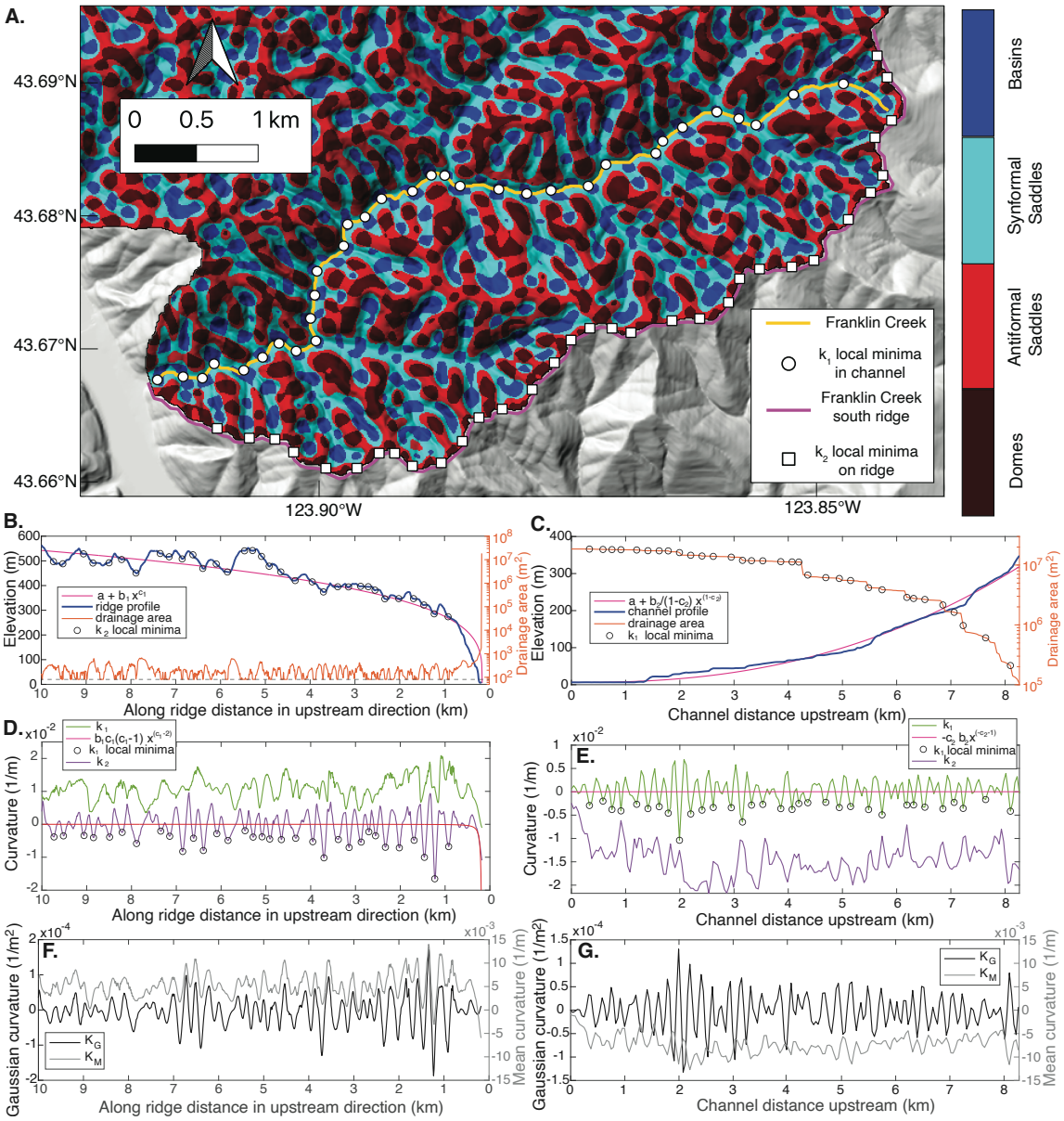

Figure 14. Characteristics of Franklin Creek and its south ridge. (a) Curvature shape classes with channel and ridge highlighted in yellow and magenta. Circles are local minima of along-channel principal curvature k_1 while squares are local minima of along-ridge principal curvature k_2. **(b)** Ridge elevation profile (left axis) and drainage area (right axis). Dashed line is drainage area for one cell. Pink curve is a powerlaw fit (fit parameters are listed in text). **(c)** Channel elevation profile (left axis) and drainage area (right axis). Pink curve is a powerlaw fit. **(d)** Principal curvatures along the south ridge. Note that local minima in k_2 (black circles) correspond to local saddles directly upslope from 1st order channel heads in (a). The mean of $k_1 = 0.01$ m^{-1} and the mean of $k_2 = -3.49 \times 10^{-4}$ m^{-1}. **(e)** Principal curvatures along Franklin Creek. Note that local minima in k_1 (black circles) correspond to junctions between tributary channels in (a). The mean of $k_1 = 8.32 \times 10^{-5}$ m^{-1} and the mean of $k_2 = -0.01$ m^{-1}. The red curve comes from stream power (it has a mean value of 1.10×10^{-5} m^{-1}). **(f)** and **(g)** Profiles of Gaussian curvature K_G and Mean curvature K_M along ridge and channel.

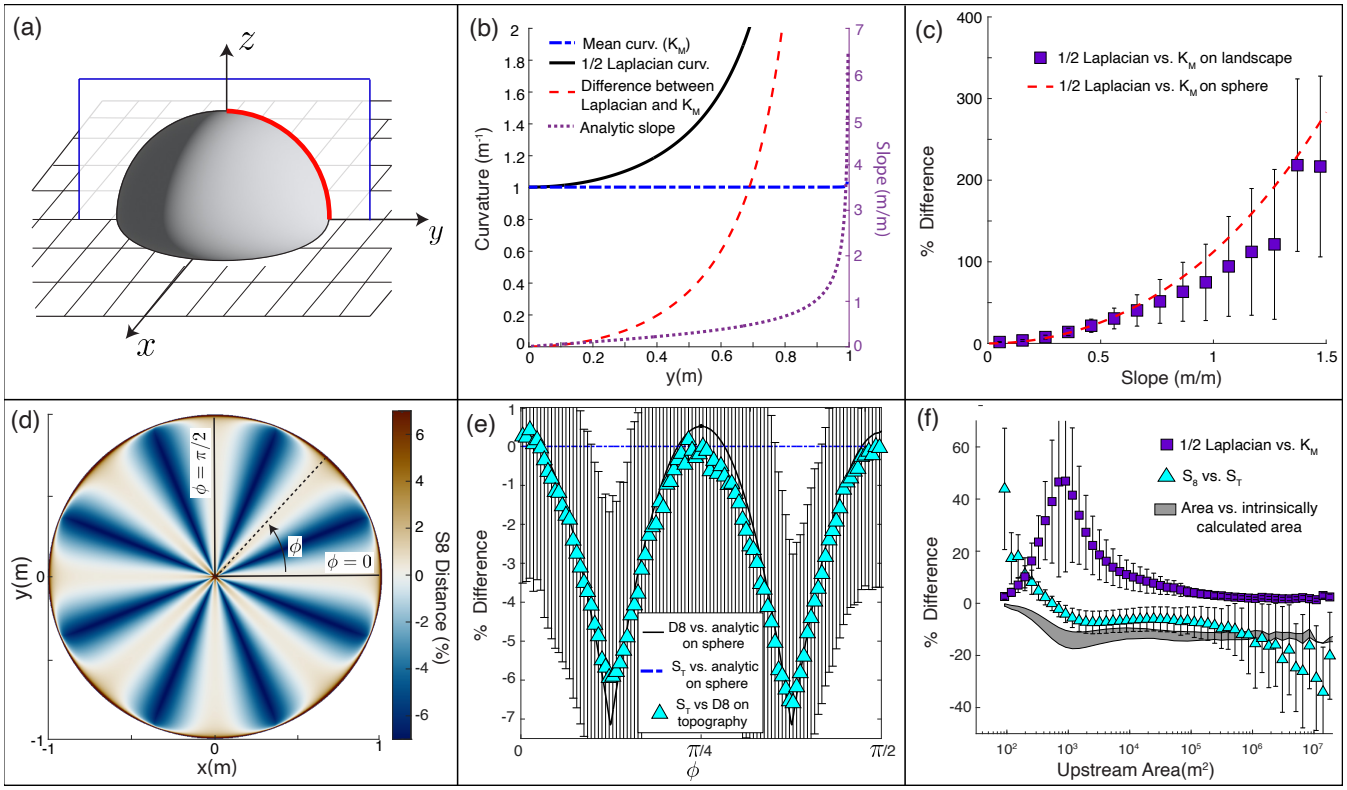

Figure 15. **Comparison of intrinsic surface metrics use in this study with other methods common in the literature. a.** Cartoon depiction of unit hemisphere used for comparison with topographic data. Red line shows curve along which error is evaluated in panel b. **b.** Comparison of Mean curvature (K_M) and $1/2$ Laplacian as a function of distance from the origin for plane curve defined by the intersection of the unit hemisphere with the $y-z$ plane. Black line is $1/2$ Laplacian, blue dashed line is Mean curvature calculated using intrinsic method, red dashed line is difference between $1/2$ Laplacian curvature and the curvature of the sphere ($1\ m^{-1}$), and the purple dashed line is slope of the sphere. **c.** $\%$ error of the $1/2$ Laplacian on the unit hemisphere and $\%$ difference between the $1/2$ Laplacian and Mean curvature on topography binned as a function of slope. Red dashed line is $\%$ error on sphere and purple boxes are median values computed on topography. **d.** $\%$ error of the 8 point connected gradient computed on the unit hemisphere. **e.** $\%$ error of the 8 point connected gradient computed on the unit hemisphere and median $\%$ difference between S_8 and S_T as a function of azimuth. **f.** $\%$ difference between our intrinsically calculated topographic metrics and other common methods as a function of drainage area.

principal curvatures)

$$K_M = \frac{1}{2}\nabla^2 z. \tag{30}$$

However, deviations in orthogonality between coordinates on a map grid, and warping of distances in regions of high slope (Fig. 2), manifest in well-known projection errors (Minár et al., 2020; Bergbauer and Pollard, 2003). Figure 15.b and c compare the half-Laplacian calculated on a coordinate grid to the invariant mean curvature on a unit hemisphere and binned topographic data respectively. The observed slope-dependent deviation of the half-Laplacian from true curvature is dramatic in end-member cases but not of concern in many studies. It can be strategically avoided by focusing on low-slope regions (Struble et al., 2024) , or evaluating curvature along 1-D hillslope profiles in which it is easier to account for slope effects (Roering et al., 2007). In addition, non-linear hillslope transport models only predict a direct correlation between curvature and erosion rates where slope is less than 30% or so, justifying the use of map-view Laplacian in regions where projection distortion is negligible (Hurst et al., 2012b; Struble et al., 2024).

A formal approach has potential to strengthen such studies, however. In reality, there are few points in the landscape with zero slope. For example, the hilltop region identified in this study makes up 18% of the landscape (Sect. 8; Fig. 8). Roughly half of this subset is at slopes above 0.4, where slope distortion in the Laplacian is around 20% (Fig. 15b-c). Selecting lower slope thresholds increases accuracy, but at the cost of data volume, a tradeoff that does not need to be considered with intrinsic approaches.

Being able to accurately sample curvature in 2-D across the hilltop-hillslope transition could also aid understanding of non-linear hillslope transport processes (Andrews and Bucknam, 1987; Roering et al., 1999b). While this transition can be analyzed through 1-D profile analysis (Roering et al., 2007), this requires careful selection of hilltop profiles and limits the volume of land-surface information that can be utilized. The ability to accurately calculate surface curvature in 2-D and put this transition in a statistical, area-space framework could help connect 1-D models to densely sampled 2-D curvature values across complicated landscapes. It can also possibly simplify other approaches that leverage local coordinate systems to explore hillslope geometry (e.g. Bonetti et al. (2018)) by allowing for the use of the xy grid rather than other local coordinate vectors in calculating intrinsic metrics.

6.2 Comparison of tangent slope to 8-connected neighborhood gradient

Our approach to computing curvatures requires definition of a unit normal vector at every DEM grid cell, which also defines the slope of the local tangent plane (S_T). We compare this method, which is mathematically equivalent to finding a slope magnitude using the Pythagorean sum of directional derivatives, to the commonly used 8-connected neighborhood gradient ($D8$) that is the default in some landscape analysis toolboxes (Schwanghart and Scherler, 2014; Mudd et al., 2019). The $D8$ method assigns a given pixel the slope between it and its lowest neighbor, providing an efficient flow routing algorithm

(O'Callaghan and Mark, 1984). However, there are systematic deviations of this metric from true slopes at certain surface orientations. Figure 15.d shows the percent difference between the $D8$ algorithm and true slope on the map-view projection of the unit sphere. Figure 15.e bins this deviation by azimuth (black line) and presents a comparison with both S_T on the sphere (blue dashed line), and the difference between S_t and $D8$ on topography (cyan triangles).

Differences between $D8$-values and the analytic slope vary systematically with orientation of the surface up to magnitudes of $\sim 7\%$. The percent error in S_T on the sphere is near zero, while the differences between the various slope metrics on topography track the same azimuthal trend. This arises because the D8-algorithm tends to underestimate slope if pixels are miss-aligned with the direction of steepest descent. We bin the percent difference between S_T and $D8$ by drainage area to track differences in the two metrics through the fluvial network (Fig. 15.f). The highest magnitude errors ($\sim 35\%$) occur on ridges (Sect. 5.1.1), while the next highest magnitude negative errors ($|> 20\%|$) occur at the highest drainage areas within the fluvial network (Sect. 5.1.4). Correlation with K_M (Fig 7) suggests sensitivity of the $D8$-algorithm to surface curvature as well as orientation.

6.3 Drainage surface area versus map-view area

As outlined in Sect. 3, this work is partially motivated by the fact that distances and areas on a sloped surface are greater than on their map-view representations. Specifically, the ratio of surface to pixel area can be calculated using the metric coefficients as $\alpha = \sqrt{EG - F}$. To evaluate the effect of projection on drainage area values, we compute two separate area grids using the D-infinity flow routing algorithm in TopoToolbox (Schwanghart and Scherler, 2014), one with uniform pixel dimensions and another where pixels are weighted by α. We bin the percent difference between these values by drainage area, with results shown in Fig. 15.f. Through most of the landscape, extrinsic drainage area calculations underestimate drainage surface area by $10 - 15\%$.

There is an extensive literature on drainage area calculation, and drainage values are known to be sensitive to grid resolution (Bernard et al., 2022), filtering scale (Erdbrügger et al., 2021), and the choice of flow routing algorithm (Tarboton, 1997). It is beyond the scope of this study to systematically integrate our intrinsic approach with other sensitivities. We will simply point out that true land surface area is derivable from DEMs, and could be beneficial in some applications. For example, efforts to define drainage-scale hydrologic responses to snow melt in mountain basins depend on estimated snow water equivalent values interpolated over topography (Chen et al., 2022; Acharki et al., 2025); models that consider groundwater infiltration and soil carbon sequestration in addition to overland flow contain parameters that depend on land surface area (Taherian and Ameli, 2026; Hunter et al., 2024); and certain definitions of characteristic topographic length scales depend on measures of area accumulation defined on the surface (Gallant and Hutchinson, 2011; Grieve et al., 2016; Kargère et al., 2024) . In each of these cases, the ability to accurately define surface area from map-view DEMs could be beneficial, though efforts to implement true surface area into process models has been shown to be inappropriate in some process model studies (e.g. Iverson and George (2024)).

7 Future directions

Quantitative classification of landforms and topography generally is challenged by the myriad interacting physical processes shaping landscapes at a range of spatial and temporal scales. Nevertheless, certain ~~geomorphic~~ metrics such as local slope and ~~upstream~~ drainage area have, through extensive empirical validation, proven to be useful indicators of spatial process transitions (Montgomery and Foufoula-Georgiou, 1993; Rosenbloom and Anderson, 1994; Stock and Dietrich, 2003) and transient landscape evolution (Kirby and Whipple, 2012; Royden and Perron, 2013).

While it is premature to claim that the curvature invariants used here have similar broad utility across landscapes, in our Coast Range study area these metrics – referenced to drainage area through Σ_G^j and Σ_M^j thresholds (Figs. 8-13) – separate the landscape into regimes that can be clearly associated with well known geomorphic processes. The Σ_G^j ~~,~~ and Σ_M^j are separated by area-space inflection points (zero crossings) in Gaussian and ~~Mean~~ mean curvature and appear to be minimally sensitive to DEM quality or smoothing. These Σ_i^j regimes, reflecting areas dominated by different combinations of convex and concave shape classes, should occur in all landscapes because they encode a distribution of 'critical points' that characterize stability and continuity in all 2D surfaces ~~(Matsumoto, 2001; Goldsten et al., 2002)~~(Matsumoto, 2001; Goldsten et al., 2002; Bonetti et al., 2018) . These geometries have implications for the sensitivity of landforms to external perturbation (Goldsten et al., 2002), and so we ~~expect that comparison of the~~ hypothesize that variation in drainage area values associated with Σ_i^j domains – perhaps in particular the concavity transition between Σ_M^0 and Σ_M^1 – ~~to~~ may reflect signatures of landscape disequilibrium.

More broadly, the presence of persistent curvature patterns in structures of interest suggest the potential for new insights into geomorphic processes. For example, oscillations in principal curvatures within fluvial channels (Σ_G^3 and Fig. 14) capture a step-pool morphology that is well documented in field studies (Grant et al., 1990; Montgomery and Buffington, 1997; Chartrand et al., 2011). This channel morphology is not explained by landscape evolution ~~studies~~ models that equate erosion rates to in-channel shear stress averaged over large spatio-temporal scales (Whipple and Tucker, 1999), but we show here that these oscillations are first order features of fluvial channel networks in the Oregon Coast Range. While the magnitude of these oscillations in curvature would need to be validated by field studies before any quantitative connections to process could be defined, the ability to potentially detect step-pool morphology at the landscape scale could open the door to connecting localized models of mass transport in rivers to landscape scale erosion models applied to topographic datasets (Venditti et al., 2020; Church and Zimmermann, 2007; Scheingross and Lamb, 2017; González et al., 2017; Escauriaza et al., 2023). In addition, the discernible valley widening signal discussed in Sect. 5.3 could aid understanding of known correlations between valley width and other landscape parameters (Bernard et al., 2022; Turowski et al., 2024).

Similarly, the ability to robustly identify colluvial hollows (a prominent component of Σ_G^2), where the topographic surface is shaped by a superposition of competing processes at the onset of convergent topography (Dietrich et al., 1993), illustrates the power of this approach. In landscape regions ~~strongly~~ shaped by debris flow processes (Struble et al., 2023), strongly disequilibrium dynamics (Donahue et al., 2013), glacial erosion (Kober et al., 2019), or even those dominated by constructional landforms such as in volcanic terrane (Karlstrom et al., 2025), slope-area scaling and other commonly used process-oriented

classification approaches break down and tools such as developed here are likely to be useful. Because surface curvature also influences shallow subsurface stress state for rock fracture (Martel, 2011; Clair et al., 2015; Moon et al., 2017) and the hydraulic gradients driving groundwater flow (Wörman et al., 2006; Zhang et al., 2022), we expect that problems in Critical Zone science may also be examined through the lens of topographic curvature (Riebe et al., 2017).

Many processes driving landscape evolution have an intrinsic scale length (Wegmann et al., 2007; Crozier et al., 2018; Roering et al., 2010), so the combination of ~~careful~~ spectral filtering to isolate certain topographic features with curvature analysis seems a promising direction for future efforts in complex geomorphic settings (Perron et al., 2008; Struble et al., 2021). For example, ~~1-d~~ 1-D measures of hillslope length in the Oregon Coast Range (Grieve et al., 2016; Roering et al., 2007) could be compared to average path lengths in the Σ_G^1 region to quantify similarities between intrinsic and extrinsic approaches, with a physically justified definition of the domain boundary given by our partitioning scheme. Quantitative comparison of our results with such ~~geometric studies that focus on~~ studies of isolated landscape domains is a clear next step in development of these methods.

From a practical standpoint, Fig. 15.f highlights how intrinsic geometric computation of topographic metrics such as slope, curvature, and ~~upstream~~ drainage area differ from the standard approach using an extrinsic map view projection of a DEM. The Σ_i^j regimes (e.g., as illustrated on Fig. 7.b) appear to be relevant. For example, curvature and drainage area computed over Σ_G^1, encompassing steep hillslopes, exhibit average ~~errors~~ differences of $\sim 50\%$ and $\sim 15\%$ respectively, which are larger than any other segment of the landscape. Slopes computed in either Σ_G^0 or Σ_G^3 ~~are maximally different by $\sim 30\%$~~, representing the smallest and largest drainage areas, are maximally different by $\sim 30\%$. Because the Σ_G^1 region accounts for the majority of land surface area (Fig. 9.a), ~~error~~ differences in drainage area from Σ_G^1 ~~persists~~ persist across all higher drainage areas with ~~error values of~~ average values $\sim 10\%$. Understanding the effects of projection distortion on empirical scaling relations (e.g., Hack's Law, Hack et al. (1957), relies on drainage area computed from a DEM), and process-based models (e.g., sediment mass-continuity ~~depends on local curvature, stream power relies on slope and drainage area,~~ and stream power Whipple and Tucker (1999)), ~~is left~~ will likely be a fruitful direction for future work~~, but we suspect it may be non-negligible in some applications~~.

Perhaps the most exciting potential developments from this approach would be in application to high resolution LiDAR data, where signatures of localized processes that drive landscape evolution can be better resolved (Roering et al., 2013). For example, it is known that hillslope processes are sensitive to bioturbation (Gabet, 2003), signatures of which cannot be resolved in the dataset used here. It is expected that the invariant approach to surface classification would be useful in resolving the topographic signatures of processes such as tree throw (Roering et al., 2010) that may heavily influence landscape-scale erosion. In the channel domain, this approach applied to LiDAR could be useful in defining the geometry of complex channel features such as waterfall plunge pools (Scheingross and Lamb, 2017).

8 Conclusions

In this work we ~~have shown how~~ build a framework using the intrinsic surface characterization approach of Carl Frederick Gauss ~~provides a powerful framework for deriving~~ to derive topographic geometry metrics for landform characterization and landscape segmentation. ~~We have shown that common metrics of topographic form, such as slope, upstream drainage area, and Laplacian-based curvature at a point are accurately captured in an intrinsic coordinate system. This approach allows us to show that errors in Laplacian curvatures are sensitive to slope and curvature, D8 slope methods are sensitive to orientation and curvature, and stream catchment area measured on the topographic surface differs by around 10% from area calculated on a map-view projection. Using results from~~ By implementing tools of classical differential geometry ~~, along with careful spectral filtering,~~ to a landscape spectrally filtered to 200 m, we show how topography ~~can be rigorously decomposed into tilings~~ at a point can be categorized as one of four shape classes, ~~which provides~~ providing a natural means of landscape segmentation that highlights channels, basins, domes, and saddles ~~.~~

(28%, 22%, 23%, and 27% of the landscape respectively). We then show through an application to the Oregon Coast Range that ~~calculation of the full curvature tensor~~ the distribution of curvature invariants reveals details about the geometric evolution of fluvial systems that go beyond that captured by standard slope-area methods. We partition the ~~landscape into segments~~ area-space landscape into four domains based on the sign of the ~~curvature invariants~~Gaussian curvature ($\Sigma_G^0 - \Sigma_G^3$), and show how these ~~segments, and the implied shape class distributions, map well on to previously known geomorphic process regimes. Accurately mapping~~ partitions correspond to previously identified geomorphic process domains. Mapping mean curvature over the entire landscape reveals a remarkable symmetry ~~in Mean curvature~~ that is reflected in ~~both the total landscapes curvature distribution and~~ total landscape curvature and slope distributions, and in the profile ~~curvature~~ curvatures measured along ridge/channel networks~~, which we hypothesize reflect signatures~~ . We hypothesize that such symmetry reflects a signature of steady-state fluvial topography. Lastly, we show that oscillations in curvatures perpendicular to channels and ridges is expressed in a regular geometric pattern that encode transitions in both concave and convex topography.

Code and data availability. The code used for data analysis is available at https://github.com/ntklema/TopoCurve_Matlab. The DEM data used in this study is available for download from The National Map at https://apps.nationalmap.gov/downloader/.

Author contributions. Conceptualization: NK, LK, Methodology: NK and LK, Visualization: NK and LK, Writing - original draft: NK, LK, and JR.

Competing interests. NK is a member of the editorial board of Geomorphica.

Acknowledgements. LK acknowledges support from NSF CAREER 1848554. LK acknowledges discussions with Jim Isenberg and with Ian Mynatt, who in different ways inspired interests in the differential geometry of geological surfaces. NK acknowledges that this work benefited from discussions with William Struble, Brooke Hunter, and Katharine Cashman.

References

Acharki, S., Boudhar, A., Bouihrouchane, A., Bousbaa, M., Karaoui, I., Elyoussfi, H., Bargam, B., Khalki, E. M. E., Hadri, A., and Chehbouni, A.: Spatial modeling of snow water equivalent in the high atlas mountains via a lumped process-based approach, Scientific Reports, 15, 26 327, https://doi.org/10.1038/s41598-025-12163-8, 2025.

Amundson, R., Heimsath, A., Owen, J., Yoo, K., and Dietrich, W. E.: Hillslope soils and vegetation, Geomorphology, 234, 122–132, https://doi.org/10.1016/j.geomorph.2014.12.031, 2015.

Andrews, D. J. and Bucknam, R. C.: Fitting degradation of shoreline scarps by a nonlinear diffusion model, Journal of Geophysical Research: Solid Earth, 92, 12 857–12 867, https://doi.org/10.1029/jb092ib12p12857, 1987.

Baldwin, E. M.: Geologic map of the lower Umpqua River area, Oregon, Tech. rep., US Geological Survey, 1961.

Bater, C. W. and Coops, N. C.: Evaluating error associated with lidar-derived DEM interpolation, Computers and Geosciences, 35, 289–300, https://doi.org/10.1016/j.cageo.2008.09.001, 2009.

Beaulieu, J. D. and Hughes, P. W.: Environmental geology of western Coos and Douglas counties, Oregon, Tech. rep., State of Oregon, Department of Geology and Mineral Industries, 1975.

Bergbauer, S. and Pollard, D. D.: How to calculate normal curvatures of sampled geological surfaces, Journal of Structural Geology, 25, 277–289, https://doi.org/10.1016/s0191-8141(02)00019-6, 2003.

Bernard, T. G., Davy, P., and Lague, D.: Hydro-Geomorphic Metrics for High Resolution Fluvial Landscape Analysis, Journal of Geophysical Research: Earth Surface, 127, https://doi.org/10.1029/2021jf006535, 2022.

Black, B. A., Perron, J. T., Hemingway, D., Bailey, E., Nimmo, F., and Zebker, H.: Planetary topography: Global drainage patterns and the origins of topographic relief on Earth, Mars, and Titan, Science, 356, 727–731, https://doi.org/10.1126/science.aag0171, 2017.

Bonetti, S., Bragg, A. D., and Porporato, A.: On the theory of drainage area for regular and non-regular points, Proceedings of the Royal Society A: Mathematical, Physical and Engineering Sciences, 474, 20170 693, https://doi.org/10.1098/rspa.2017.0693, 2018.

Bonetti, S., Hooshyar, M., Camporeale, C., and Porporato, A.: Channelization cascade in landscape evolution, Proceedings of the National Academy of Sciences, 117, 1375–1382, https://doi.org/10.1073/pnas.1911817117, 2020.

Booth, A. M., Roering, J. J., and Perron, J. T.: Automated landslide mapping using spectral analysis and high-resolution topographic data: Puget Sound lowlands, Washington, and Portland Hills, Oregon, Geomorphology, 109, 132–147, https://doi.org/10.1016/j.geomorph.2009.02.027, 2009.

Brigham, C. A. and Crider, J. G.: A new metric for morphologic variability using landform shape classification via supervised machine learning, Geomorphology, 399, 108 065, https://doi.org/10.1016/j.geomorph.2021.108065, 2022.

Bui, L. K. and Glennie, C. L.: Estimation of lidar-based gridded DEM uncertainty with varying terrain roughness and point density, ISPRS Open Journal of Photogrammetry and Remote Sensing, 7, 100 028, https://doi.org/10.1016/j.ophoto.2022.100028, 2023.

Cayley: XL. On contour and slope lines, The London, Edinburgh, and Dublin Philosophical Magazine and Journal of Science, 18, 264–268, https://doi.org/10.1080/14786445908642760, 1859.

Chartrand, S. M., Jellinek, M., Whiting, P. J., and Stamm, J.: Geometric scaling of step-pools in mountain streams: Observations and implications, Geomorphology, 129, 141–151, https://doi.org/10.1016/j.geomorph.2011.01.020, 2011.

Chen, X., Tang, G., Chen, T., and Niu, X.: An Assessment of the Impacts of Snowmelt Rate and Continuity Shifts on Streamflow Dynamics in Three Alpine Watersheds in the Western U.S., Water, 14, 1095, https://doi.org/10.3390/w14071095, 2022.

Church, M. and Zimmermann, A.: Form and stability of step-pool channels: Research progress, Water Resources Research, 43, 1–21, https://doi.org/10.1029/2006wr005037, 2007.

Clair, J. S., Moon, S., Holbrook, W. S., Perron, J. T., Riebe, C. S., Martel, S. J., Carr, B., Harman, C., Singha, K., and Richter, D. d.: Geophysical imaging reveals topographic stress control of bedrock weathering, Science, 350, 534–538, https://doi.org/10.1126/science.aab2210, 2015.

Cogliati, A. and Rivis, R.: The origins of the fundamental theorem of surface theory, Historia Mathematica, 61, 45–79, https://doi.org/10.1016/j.hm.2022.09.001, 2022.

Crosby, C. J., Arrowsmith, J. R., and Nandigam, V.: Chapter 11 Zero to a trillion: Advancing Earth surface process studies with open access to high-resolution topography, Developments in Earth Surface Processes, 23, 317–338, https://doi.org/10.1016/b978-0-444-64177-9.00011-4, 2020.

Crozier, J., Karlstrom, L., and Yang, K.: Basal control of supraglacial meltwater catchments on the Greenland Ice Sheet, The Cryosphere, 12, 3383–3407, https://doi.org/10.5194/tc-12-3383-2018, 2018.

Culling, W. E. H.: Analytical Theory of Erosion, The Journal of Geology, 68, 336–344, https://doi.org/10.1086/626663, 1960.

Daly, C. and Bryant, K.: The PRISM Climate and Weather System – An Introduction, Corvallis, OR: PRISM climate group 2, 2013.

Davis, A. W. M.: The Convex Profile of Bad-Land Divides, Science, 20, 27–28, 1892.

Dekking, F. M., Kraaikamp, C., Lopuhaä, H. P., and Meester, L. E.: A Modern Introduction to Probability and Statistics, Understanding Why and How, ISBN 9781852338961, https://doi.org/10.1007/1-84628-168-7, 2005.

Deshpande, N. S., Furbish, D. J., Arratia, P. E., and Jerolmack, D. J.: The perpetual fragility of creeping hillslopes, Nature Communications, 12, 3909, https://doi.org/10.1038/s41467-021-23979-z, 2021.

Dietrich, W. E. and Dunne, T.: Sediment budget for a small catchment in a mountainous terrain, Routledge: London, UK, 1978.

Dietrich, W. E., Wilson, C. J., Montgomery, D. R., and McKean, J.: Analysis of Erosion Thresholds, Channel Networks, and Landscape Morphology Using a Digital Terrain Model, The Journal of Geology, 101, 259–278, https://doi.org/10.1086/648220, 1993.

Donahue, M. S., Karlstrom, K. E., Aslan, A., Darling, A., Granger, D., Wan, E., Dickinson, R. G., and Kirby, E.: Incision history of the Black Canyon of Gunnison, Colorado, over the past ~ 1 Ma inferred from dating of fluvial gravel deposits, Geosphere, 9, 815–826, https://doi.org/10.1130/ges00847.1, 2013.

Einstein, A. and Lawson, R. W.: Relativity, The Special and the General Theory, Man and the Universe, 1 (series, 56–58, https://doi.org/10.4324/9781315886749-18, 2013.

Erdbrügger, J., Meerveld, I. v., Bishop, K., and Seibert, J.: Effect of DEM-smoothing and -aggregation on topographically-based flow directions and catchment boundaries, Journal of Hydrology, 602, 126 717, https://doi.org/10.1016/j.jhydrol.2021.126717, 2021.

Escauriaza, C., González, C., Williams, M. E., and Brevis, W.: Models of bed-load transport across scales: turbulence signature from grain motion to sediment flux, Stochastic Environmental Research and Risk Assessment, 37, 1039–1052, https://doi.org/10.1007/s00477-022-02333-9, 2023.

Fenneman, N.: Some Features of Erosion by Unconcentrated Wash, The Journal of Geology, 16, 746–754, 1908.

Fernandes, N. F. and Dietrich, W. E.: Hillslope evolution by diffusive processes: The timescale for equilibrium adjustments, Water Resources Research, 33, 1307–1318, https://doi.org/10.1029/97wr00534, 1997.

Ferrier, K. L., Huppert, K. L., and Perron, J. T.: Climatic control of bedrock river incision, Nature, 496, 206–209, https://doi.org/10.1038/nature11982, 2013.

Flint, J. J.: Stream gradient as a function of order, magnitude, and discharge, Water Resources Research, 10, 969–973, https://doi.org/10.1029/wr010i005p00969, 1974.

Furbish, D. J., Haff, P. K., Dietrich, W. E., and Heimsath, A. M.: Statistical description of slope-dependent soil transport and the diffusion-like coefficient, Journal of Geophysical Research: Earth Surface, 114, https://doi.org/10.1029/2009jf001267, 2009.

Gabet, E. J.: Sediment transport by dry ravel, Journal of Geophysical Research: Solid Earth, 108, https://doi.org/10.1029/2001jb001686, 2003.

Gallant, J.: Adaptive smoothing for noisy DEMs, Geomorphometry, 2011, 7–9, 2011.

Gallant, J. C. and Hutchinson, M. F.: A differential equation for specific catchment area, Water Resources Research, 47, https://doi.org/10.1029/2009wr008540, 2011.

Gauss, C. F.: General Investigations of Curved Surfaces of 1827 and 1825, Nature, 66, 316–317, https://doi.org/10.1038/066316b0, 1902.

Gilbert, G. K.: Geology of the Henry Mountains, U.S. Geographical and Geological Survey of the Rocky Mountain Region, p. 196, 1877.

Gilbert, G. K.: The Convexity of Hilltops, The Journal of Geology, 17, 344–350, 1908.

Goldsten, H., Safko, J., and Poole, C.: Classical Mechanics, Addison-Wesley, 3rd edn., 2002.

González, C., Richter, D. H., Bolster, D., Bateman, S., Calantoni, J., and Escauriaza, C.: Characterization of bedload intermittency near the threshold of motion using a Lagrangian sediment transport model, Environmental Fluid Mechanics, 17, 111–137, https://doi.org/10.1007/s10652-016-9476-x, 2017.

Grant, G. E., Swanson, F. J., and Wolman, M. G.: Pattern and origin of stepped-bed morphology in high-gradient streams, Western Cascades, Oregon, GSA Bulletin, 102, 340–352, https://doi.org/10.1130/0016-7606(1990)102<0340:paoosb>2.3.co;2, 1990.

Grieve, S. W., Mudd, S. M., and Hurst, M. D.: How long is a hillslope?, Earth Surface Processes and Landforms, 41, 1039–1054, https://doi.org/10.1002/esp.3884, 2016.

Hack, J. T., Seaton, F. A., and Nolan, T. B.: Studies of Longitudinal Stream Profiles in Virginia and Maryland, vol. 294, US Government Printing Office, 1957.

Han, L. and Che, S.: An Overview of Materials with Triply Periodic Minimal Surfaces and Related Geometry: From Biological Structures to Self-Assembled Systems, Advanced Materials, 30, e1705 708, https://doi.org/10.1002/adma.201705708, 2018.

Harris, F. J.: On the Use of Windows for Harmonic Analysis with the Discrete Fourier Transform, Proceedings of the IEEE, 66, 51–83, https://doi.org/10.1109/proc.1978.10837, 1978.

Heideman, M. T., Johnson, D. H., and Burrus, C. S.: Gauss and the history of the fast Fourier transform, Archive for History of Exact Sciences, 34, 265–277, https://doi.org/10.1007/bf00348431, 1985.

Heimsath, A. M., Dietrich, W. E., Nishiizumi, K., and Finkel, R. C.: Stochastic processes of soil production and transport: erosion rates, topographic variation and cosmogenic nuclides in the Oregon Coast Range, Earth Surface Processes and Landforms, 26, 531–552, https://doi.org/10.1002/esp.209, 2001.

Hooshyar, M., Bonetti, S., Singh, A., Foufoula-Georgiou, E., and Porporato, A.: From turbulence to landscapes: Logarithmic mean profiles in bounded complex systems, Physical Review E, 102, 033 107, https://doi.org/10.1103/physreve.102.033107, 2020.

Hunter, B. D., Roering, J. J., Silva, L. C. R., and Moreland, K. C.: Geomorphic controls on the abundance and persistence of soil organic carbon pools in erosional landscapes, Nature Geoscience, 17, 151–157, https://doi.org/10.1038/s41561-023-01365-2, 2024.

Hurst, M. D., Mudd, S. M., Walcott, R., Attal, M., and Yoo, K.: Using hilltop curvature to derive the spatial distribution of erosion rates, Journal of Geophysical Research: Earth Surface, 117, 1–19, https://doi.org/10.1029/2011jf002057, 2012a.

Hurst, M. D., Mudd, S. M., Walcott, R., Attal, M., and Yoo, K.: Using hilltop curvature to derive the spatial distribution of erosion rates, Journal of Geophysical Research: Earth Surface, 117, https://doi.org/10.1029/2011jf002057, 2012b.

Iverson, R. M. and George, D. L.: Advances in Debris-flow Science and Practice, Geoenvironmental Disaster Reduction, pp. 127–163, https://doi.org/10.1007/978-3-031-48691-3_5, 2024.

Jaeger, H. M. and Nagel, S. R.: Physics of the Granular State, Science, 255, 1523–1531, https://doi.org/10.1126/science.255.5051.1523, 1992.

Jasiewicz, J. and Stepinski, T. F.: Geomorphons — a pattern recognition approach to classification and mapping of landforms, Geomorphology, 182, 147–156, https://doi.org/10.1016/j.geomorph.2012.11.005, 2013.

Jordan, G.: Adaptive smoothing of valleys in DEMs using TIN interpolation from ridgeline elevations: An application to morphotectonic aspect analysis, Computers & Geosciences, 33, 573–585, https://doi.org/10.1016/j.cageo.2006.08.010, 2007.

Kargère, B. A., Constantine, J. A., Hales, T. C., Grieve, S. W. D., and Johnson, S. D.: A Fractal Framework for Channel-Hillslope Coupling, EGUsphere, 2024, 1–24, https://doi.org/10.5194/egusphere-2024-2847, 2024.

Karlstrom, L., Klema, N., Grant, G. E., Finn, C., Sullivan, P. L., Cooley, S., Simpson, A., Fasth, B., Cashman, K., Ferrier, K., Ball, L., and McKay, D.: State shifts in the deep Critical Zone drive landscape evolution in volcanic terrains, Proceedings of the National Academy of Sciences, 122, e2415155 122, https://doi.org/10.1073/pnas.2415155122, 2025.

Kelsey, H. M., Ticknor, R. L., Bockheim, J. G., and Mitchell, E.: Quaternary upper plate deformation in coastal Oregon, GSA Bulletin, 108, 843–860, https://doi.org/10.1130/0016-7606(1996)108<0843:qupdic>2.3.co;2, 1996.

Kirby, E. and Whipple, K. X.: Expression of active tectonics in erosional landscapes, Journal of Structural Geology, 44, 54–75, https://doi.org/10.1016/j.jsg.2012.07.009, 2012.

Kirby, J. F.: Estimation of the effective elastic thickness of the lithosphere using inverse spectral methods: The state of the art, Tectonophysics, 631, 87–116, https://doi.org/10.1016/j.tecto.2014.04.021, 2014.

Klema, N., Karlstrom, L., Cannon, C., Jiang, C., O'Connor, J., Wells, R., and Schmandt, B.: The magmatic origin of the Columbia River Gorge, USA, Science Advances, 9, eadj3357, https://doi.org/10.1126/sciadv.adj3357, 2023.

Kober, F., Hippe, K., Salcher, B., Grischott, R., Zurfluh, R., Hajdas, I., Wacker, L., Christl, M., and Ivy-Ochs, S.: Postglacial to Holocene landscape evolution and process rates in steep alpine catchments, Earth Surface Processes and Landforms, 44, 242–258, https://doi.org/10.1002/esp.4491, 2019.

LaHusen, S. R., Duvall, A. R., Booth, A. M., Grant, A., Mishkin, B. A., Montgomery, D. R., Struble, W., Roering, J. J., and Wartman, J.: Rainfall triggers more deep-seated landslides than Cascadia earthquakes in the Oregon Coast Range, USA, Science Advances, 6, eaba6790, https://doi.org/10.1126/sciadv.aba6790, 2020.

Luu, C., Forino, G., Yorke, L., Ha, H., Bui, Q. D., Tran, H. H., Nguyen, D. Q., Duong, H. C., and Kervyn, M.: Integrating susceptibility maps of multiple hazards and building exposure distribution: a case study of wildfires and floods for the province of Quang Nam, Vietnam, Natural Hazards and Earth System Sciences, 24, 4385–4408, https://doi.org/10.5194/nhess-24-4385-2024, 2024.

Martel, S. J.: Mechanics of curved surfaces, with application to surface-parallel cracks, Geophysical Research Letters, 38, n/a–n/a, https://doi.org/10.1029/2011gl049354, 2011.

Matsumoto, Y.: An Introduction to Morse Theory, Translations of Mathematical Monographs, pp. 33–72, https://doi.org/10.1090/mmono/208/02, 2001.

Maxwell, J. C.: L. on hills and dales: To the editors of the philosophical magazine and journal, The London, Edinburgh, and Dublin Philosophical Magazine and Journal of Science, 40, 421–427, https://doi.org/10.1080/14786447008640422, 1870.

Mcguire, L. A., Mccoy, S. W., Marc, O., Struble, W., and Barnhart, K. R.: Steady-state forms of channel profiles shaped by debris-flow and fluvial processes, Earth Surface Dynamics Discussions, pp. 1–33, https://doi.org/10.5194/esurf-2022-47, 2022.

McNeill, L. C., Goldfinger, C., Kulm, L. D., and Yeats, R. S.: Tectonics of the Neogene Cascadia forearc basin: Investigations of a deformed late Miocene unconformity, GSA Bulletin, 112, 1209–1224, https://doi.org/10.1130/0016-7606(2000)112<1209:totncf>2.0.co;2, 2000.

Mcnutt, M.: Influence Of Plate Subduction On Isostatic Compensation in Northern California, Tectonics, 4, 399–415, 1983.

Minár, J., Evans, I. S., and Jenčo, M.: A comprehensive system of definitions of land surface (topographic) curvatures, with implications for their application in geoscience modelling and prediction, Earth-Science Reviews, 211, 103 414, https://doi.org/10.1016/j.earscirev.2020.103414, 2020.

Montgomery, D. R.: Slope Distributions, Threshold Hillslopes, and Steady-state Topography, American Journal of Science, 301, 432–454, https://doi.org/10.2475/ajs.301.4-5.432, 2001.

Montgomery, D. R. and Buffington, J. M.: Channel-reach morphology in mountain drainage basins, GSA Bulletin, 109, 596–611, https://doi.org/10.1130/0016-7606(1997)109<0596:crmimd>2.3.co;2, 1997.

Montgomery, D. R. and Foufoula-Georgiou, E.: Channel network source representation using digital elevation models, Water Resources Research, 29, 3925–3934, https://doi.org/10.1029/93wr02463, 1993.

Moon, S., Perron, J. T., Martel, S. J., Holbrook, W. S., and Clair, J. S.: A model of three-dimensional topographic stresses with implications for bedrock fractures, surface processes, and landscape evolution, Journal of Geophysical Research: Earth Surface, 122, 823–846, https://doi.org/10.1002/2016jf004155, 2017.

Mudd, S. M., Gailleton, B., Clubb, F., Grieve, S., and Valters, D.: LSDTopoTools2 v2.01 (Version v2.01), http://doi.org/10.5281/zenodo.3245076, 2019.

Mynatt, I., Bergbauer, S., and Pollard, D. D.: Using differential geometry to describe 3-D folds, Journal of Structural Geology, 29, 1256–1266, https://doi.org/10.1016/j.jsg.2007.02.006, 2007.

Needham, T.: Visual Differential Geometry and Forms: A Mathematical Drama in Five Acts, Princeton University Press, Princeton, 2021.

O'Callaghan, J. F. and Mark, D. M.: The extraction of drainage networks from digital elevation data, Computer Vision, Graphics, and Image Processing, 28, 323–344, https://doi.org/10.1016/s0734-189x(84)80011-0, 1984.

O'Hara, D., Karlstrom, L., and Roering, J. J.: Distributed landscape response to localized uplift and the fragility of steady states, Earth and Planetary Science Letters, 506, 243–254, https://doi.org/10.1016/j.epsl.2018.11.006, 2019.

O'Neill, B.: Elementary differential geometry, Elementary differential geometry, 2006.

Osserman, R.: A survey of minimal surfaces, Courier Corporation, 2013.

Passalacqua, P., Trung, T. D., Foufoula-Georgiou, E., Sapiro, G., and Dietrich, W. E.: A geometric framework for channel network extraction from lidar: Nonlinear diffusion and geodesic paths, Journal of Geophysical Research: Earth Surface, 115, https://doi.org/10.1029/2009jf001254, 2010.

Pearce, M. A., Jones, R. R., Smith, S. A., McCaffrey, K. J., and Clegg, P.: Numerical analysis of fold curvature using data acquired by high-precision GPS, Journal of Structural Geology, 28, 1640–1646, https://doi.org/10.1016/j.jsg.2006.05.010, 2006.

Perron, J. T., Kirchner, J. W., and Dietrich, W. E.: Spectral signatures of characteristic spatial scales and nonfractal structure in landscapes, Journal of Geophysical Research: Earth Surface, 113, https://doi.org/10.1029/2007jf000866, 2008.

Perron, J. T., Kirchner, J. W., and Dietrich, W. E.: Formation of evenly spaced ridges and valleys, Nature, 460, 502–505, https://doi.org/10.1038/nature08174, 2009.

Perron, J. T., Richardson, P. W., Ferrier, K. L., and Lapôtre, M.: The root of branching river networks, Nature, 492, 100–103, https://doi.org/10.1038/nature11672, 2012.

Personius, S. F.: Late Quaternary stream incision and uplift in the forearc of the Cascadia subduction zone, western Oregon, Journal of Geophysical Research: Solid Earth, 100, 20 193–20 210, https://doi.org/10.1029/95jb01684, 1995.

Pesic, P.: Beyond Geometry: Classic Papers from Riemann to Einstein, Courier Corporation, 2007.

Reneau, S. L. and Dietrich, W. E.: Erosion rates in the southern oregon coast range: Evidence for an equilibrium between hillslope erosion and sediment yield, Earth Surface Processes and Landforms, 16, 307–322, https://doi.org/10.1002/esp.3290160405, 1991.

Reuter, H. I., Hengl, T., Gessler, P., and Soille, P.: Preparation of DEMs for geomorphometric analysis, Developments in Soil Science, 33, 87–120, https://doi.org/10.1016/s0166-2481(08)00004-4, 2009.

Richardson, P. and Karlstrom, L.: The multi-scale influence of topography on lava flow morphology, Bulletin of Volcanology, 81, 21, https://doi.org/10.1007/s00445-019-1278-9, 2019.

Riebe, C. S., Hahm, W. J., and Brantley, S. L.: Controls on deep critical zone architecture: a historical review and four testable hypotheses, Earth Surface Processes and Landforms, 42, 128–156, https://doi.org/10.1002/esp.4052, 2017.

Riza, S., Sekine, M., Kanno, A., Yamamoto, K., Imai, T., and Higuchi, T.: Land Suitability Analysis for Agricultural Land Use using Hyperscale DEM Data, AGRIVITA Journal of Agricultural Science, 44, https://doi.org/10.17503/agrivita.v44i2.2985, 2022.

Roering, J. J., Kirchner, J. W., and Dietrich, W. E.: Evidence for nonlinear, diffusive sediment transport on hillslopes and implications for landscape morphology, Water Resources Research, 35, 853–870, https://doi.org/10.1029/1998wr900090, 1999a.

Roering, J. J., Kirchner, J. W., and Dietrich, W. E.: Evidence for nonlinear, diffusive sediment transport on hillslopes and implications for landscape morphology, Water Resources Research, 35, 853–870, https://doi.org/10.1029/1998wr900090, 1999b.

Roering, J. J., Kirchner, J. W., and Dietrich, W. E.: Hillslope evolution by nonlinear, slope-dependent transport: Steady state morphology and equilibrium adjustment timescales, Journal of Geophysical Research: Solid Earth, 106, 16 499–16 513, https://doi.org/10.1029/2001jb000323, 2001a.

Roering, J. J., Kirchner, J. W., Sklar, L. S., and Dietrich, W. E.: Hillslope evolution by nonlinear creep and landsliding: An experimental study, Geology, 29, 143–146, https://doi.org/10.1130/0091-7613(2001)029<0143:hebnca>2.0.co;2, 2001b.

Roering, J. J., Kirchner, J. W., and Dietrich, W. E.: Characterizing structural and lithologic controls on deep-seated landsliding: Implications for topographic relief and landscape evolution in the Oregon Coast Range, USA, Bulletin of the Geological Society of America, 117, 654–668, https://doi.org/10.1130/b25567.1, 2005.

Roering, J. J., Perron, J. T., and Kirchner, J. W.: Functional relationships between denudation and hillslope form and relief, Earth and Planetary Science Letters, 264, 245–258, https://doi.org/10.1016/j.epsl.2007.09.035, 2007.

Roering, J. J., Marshall, J., Booth, A. M., Mort, M., and Jin, Q.: Evidence for biotic controls on topography and soil production, Earth and Planetary Science Letters, 298, 183–190, https://doi.org/10.1016/j.epsl.2010.07.040, 2010.

Roering, J. J., Mackey, B. H., Marshall, J. A., Sweeney, K. E., Deligne, N. I., Booth, A. M., Handwerger, A. L., and Cerovski-Darriau, C.: 'You are HERE': Connecting the dots with airborne lidar for geomorphic fieldwork, Geomorphology, 200, 172–183, https://doi.org/10.1016/j.geomorph.2013.04.009, 2013.

Rosenbloom, N. A. and Anderson, R. S.: Hillslope and channel evolution in a marine terraced landscape, Santa Cruz, California, Journal of Geophysical Research: Solid Earth, 99, 14 013–14 029, https://doi.org/10.1029/94jb00048, 1994.

Royden, L. and Perron, J. T.: Solutions of the stream power equation and application to the evolution of river longitudinal profiles, Journal of Geophysical Research: Earth Surface, 118, 497–518, https://doi.org/10.1002/jgrf.20031, 2013.

Ruh, J. B.: Numerical modeling of tectonic underplating in accretionary wedge systems, Geosphere, 16, 1385–1407, https://doi.org/10.1130/ges02273.1, 2020.

Scheingross, J. S. and Lamb, M. P.: A Mechanistic Model of Waterfall Plunge Pool Erosion into Bedrock, Journal of Geophysical Research: Earth Surface, 122, 2079–2104, https://doi.org/10.1002/2017jf004195, 2017.

Scherler, D. and Schwanghart, W.: Identification and ordering of drainage divides in digital elevation models, Earth Surface Dynamics Discussions, pp. 1–35, https://doi.org/10.5194/esurf-2019-51, 2019.

Schmidt, J., Evans, I. S., and Brinkmann, J.: Comparison of polynomial models for land surface curvature calculation, International Journal of Geographical Information Science, 17, 797–814, https://doi.org/10.1080/13658810310001596058, 2003.

Schwanghart, W. and Scherler, D.: Short Communication: TopoToolbox 2 – MATLAB-based software for topographic analysis and modeling in Earth surface sciences, Earth Surface Dynamics, 2, 1–7, https://doi.org/10.5194/esurf-2-1-2014, 2014.

Shary, P. A.: Land surface in gravity points classification by a complete system of curvatures, Mathematical Geology, 27, 373–390, https://doi.org/10.1007/bf02084608, 1995.

Sofia, G.: Combining geomorphometry, feature extraction techniques and Earth-surface processes research: The way forward, Geomorphology, 355, 107 055, https://doi.org/10.1016/j.geomorph.2020.107055, 2020.

Stewart, J.: Multivariable Calculus, Brooks Cole, 2003.

Stock, J. and Dietrich, W. E.: Valley incision by debris flows: Evidence of a topographic signature, Water Resources Research, 39, https://doi.org/10.1029/2001wr001057, 2003.

Stock, J. D. and Montgomery, D. R.: Geologic constraints on bedrock river incision using the stream power law, Journal of Geophysical Research: Solid Earth, 104, 4983–4993, https://doi.org/10.1029/98jb02139, 1999.

Struble, W. T., Roering, J. J., Dorsey, R. J., and Bendick, R.: Characteristic Scales of Drainage Reorganization in Cascadia, Geophysical Research Letters, 48, https://doi.org/10.1029/2020gl091413, 2021.

Struble, W. T., McGuire, L. A., McCoy, S. W., Barnhart, K. R., and Marc, O.: Debris-Flow Process Controls on Steepland Morphology in the San Gabriel Mountains, California, Journal of Geophysical Research: Earth Surface, 128, https://doi.org/10.1029/2022jf007017, 2023.

Struble, W. T., Clubb, F. J., and Roering, J. J.: Regional-scale, high-resolution measurements of hilltop curvature reveal tectonic, climatic, and lithologic controls on hillslope morphology, Earth and Planetary Science Letters, 647, 119 044, https://doi.org/10.1016/j.epsl.2024.119044, 2024.

Struik, D. J. D. J.: Lectures on classical differential geometry, Lectures on classical differential geometry, 1950.

Taherian, M. and Ameli, A. A.: Time Variance in Snowmelt Partitioning: A Mechanistic Modeling Approach to Explore the Role of Catchment Structure and Pre-Snow Rainfall, Water Resources Research, 62, https://doi.org/10.1029/2025wr040679, 2026.

Tarboton, D. G.: A new method for the determination of flow directions and upslope areas in grid digital elevation models, Water Resources Research, 33, 309–319, https://doi.org/10.1029/96wr03137, 1997.

Tucker, G. E., Lancaster, S. T., Gasparini, N. M., Bras, R. L., and Rybarczyk, S. M.: An object-oriented framework for distributed hydrologic and geomorphic modeling using triangulated irregular networks, Computers & Geosciences, 27, 959–973, https://doi.org/10.1016/s0098-3004(00)00134-5, 2001.

Turcotte, D. L.: A fractal interpretation of topography and geoid spectra on the Earth, Moon, Venus, and Mars, Journal of Geophysical Research: Solid Earth, 92, E597–E601, https://doi.org/10.1029/jb092ib04p0e597, 1987.

Turowski, J. M., Bufe, A., and Tofelde, S.: A physics-based model for fluvial valley width, Earth Surface Dynamics, 12, 493–514, https://doi.org/10.5194/esurf-12-493-2024, 2024.

Venditti, J. G., Li, T., Deal, E., Dingle, E., and Church, M.: Struggles with stream power: Connecting theory across scales, Geomorphology, 366, 106 817, https://doi.org/10.1016/j.geomorph.2019.07.004, 2020.

Watts, A. B.: Isostasy and flexure of the lithosphere, Cambridge University Press, Cambridge, United Kingdom, 2001.

Wegmann, K. W., Zurek, B. D., Regalla, C. A., Bilardello, D., Wollenberg, J. L., Kopczynski, S. E., Ziemann, J. M., Haight, S. L., Apgar, J. D., Zhao, C., and Pazzaglia, F. J.: Position of the Snake River watershed divide as an indicator of geodynamic processes in the greater Yellowstone region, western North America, Geosphere, 3, 272–281, https://doi.org/10.1130/ges00083.1, 2007.

Wells, R., Bukry, D., Friedman, R., Pyle, D., Duncan, R., Haeussler, P., and Wooden, J.: Geologic history of Siletzia, a large igneous province in the Oregon and Washington Coast Range: Correlation to the geomagnetic polarity time scale and implications for a long-lived Yellowstone hotspot, Geosphere, 10, 692–719, https://doi.org/10.1130/ges01018.1, 2014.

Whipple, K., DiBiase, R., and Crosby, B.: Treatise on Geomorphology, Specific Fluvial Environments, pp. 550–573, https://doi.org/10.1016/b978-0-12-374739-6.00254-2, 2013.

Whipple, K. X. and Tucker, G. E.: Dynamics of the stream-power river incision model: Implications for height limits of mountain ranges, landscape response timescales, and research needs, Journal of Geophysical Research: Solid Earth, 104, 17 661–17 674, https://doi.org/10.1029/1999jb900120, 1999.

Wieczorek, M. A.: Gravity and Topography of the Terrestrial Planets, Treatise on geophysics, 10, 165–206, https://doi.org/10.1016/b978-0-444-53802-4.00169-x, 2015.

Willett, S. D.: Erosion on a line, Tectonophysics, 484, 168–180, https://doi.org/10.1016/j.tecto.2009.09.011, 2010.

Wobus, C., Whipple, K. X., Kirby, E., Snyder, N., Johnson, J., Spyropolou, K., Crosby, B., and Sheehan, D.: Tectonics from topography: Procedures, promise, and pitfalls, Special Paper of the Geological Society of America, 398, 55–74, https://doi.org/10.1130/2006.2398(04), 2006.

Wörman, A., Packman, A. I., Marklund, L., Harvey, J. W., and Stone, S. H.: Exact three-dimensional spectral solution to surface-groundwater interactions with arbitrary surface topography, Geophysical Research Letters, 33, https://doi.org/10.1029/2006gl025747, 2006.

Yanites, B. J., Clark, M. K., Roering, J. J., West, A. J., Zekkos, D., Baldwin, J. W., Cerovski-Darriau, C., Gallen, S. F., Horton, D. E., Kirby, E., Leshchinsky, B. A., Mason, H. B., Moon, S., Barnhart, K. R., Booth, A., Czuba, J. A., McCoy, S., McGuire, L., Pfeiffer, A., and Pierce, J.: Cascading land surface hazards as a nexus in the Earth system, Science, 388, eadp9559, https://doi.org/10.1126/science.adp9559, 2025.

Zhang, X., Jiao, J. J., and Guo, W.: How Does Topography Control Topography-Driven Groundwater Flow?, Geophysical Research Letters, 49, https://doi.org/10.1029/2022gl101005, 2022.